

**MODELING AND ANALYSIS OF THE CONTROL OF INDIVIDUAL  
STACKS OF A MULTI-STACK PIEZOELECTRIC ACTUATOR  
FOR HYBRID DC CIRCUIT BREAKERS**

A Thesis  
Presented to  
The Academic Faculty

by

Amrita Ghosh

In Partial Fulfillment  
of the Requirements for the Degree  
Masters of Science in the  
School of Electrical and Computer Engineering

Georgia Institute of Technology  
May 2023

**COPYRIGHT © 2023 BY AMRITA GHOSH**

**MODELING AND ANALYSIS OF THE CONTROL OF INDIVIDUAL  
STACKS OF A MULTI-STACK PIEZOELECTRIC ACTUATOR  
FOR HYBRID DC CIRCUIT BREAKERS**

Approved by:

Dr. Lukas Graber, Advisor  
School of Electrical and Computer Engineering  
*Georgia Institute of Technology*

Dr. Maryam Saeedifard  
School of Electrical and Computer Engineering  
*Georgia Institute of Technology*

Dr. Lauren Garten  
School of Materials Science and Engineering  
*Georgia Institute of Technology*

Date Approved: April 26, 2023

*To my grandparents Nandita Mukherjee and Kartik Mukherjee,  
for their constant love and support.*

## ACKNOWLEDGEMENTS

I would like to express my heartfelt gratitude to my advisor Dr. Lukas Graber, for his unwavering support, encouragement, and guidance throughout my research journey. His insights, suggestions, and feedback have been invaluable in shaping my thesis and shaping me as a researcher.

My sincere thanks go to my thesis committee members, Dr. Maryam Saedifard and Dr. Lauren Garten, for their valuable feedback and guidance, which have greatly contributed to the development and improvement of my thesis.

It was a great experience to work with the members of the Plasma and Dielectrics Laboratory at Georgia Tech and the Center for Advanced Power Systems at Florida State University. I would like to thank them for their support and for providing a collaborative and stimulating research environment. I am grateful to my lab mates, Dr. Zhiyang Jin, Dr. Maryam Tousi, Alfonso Cruz, Ebrahim Karimi, Kevin Whitmore, Amanda West, Ning Guo, Ajay Sukhwani, and Yang Liu for their help, feedback, and encouragement throughout my research. Special thanks to Dr. Chunmeng Xu for taking the time to guide me and address my questions over the past three semesters.

I would also like to thank my friends in the ECE community at Georgia Tech for their encouragement, support, and invaluable discussions that have enriched my research experience. Thank you to Priya Mana, Kartavya Agarwal, Amogh Dabholkar, Dhruva Barfiwala, Ahmed Shaikh, Sumedh Naik, Pradeepti Gupta, Vidit Jha, Shlok Shah, Aditya Salian, and Anirudh Heda for their friendship and support.

I would like to express my deepest gratitude to my parents, Dr. Sujata Ghosh and Dr. Debasis Ghosh, for their love, support, and encouragement throughout my academic journey. Their guidance and sacrifices have been instrumental in my academic and personal growth. I am also grateful to my siblings, Debanu Ghosh and Dr. Deboshree Ghosh, for their love, companionship, and constant motivation. Above all, I would like to thank my grandparents, for their unconditional love, strength and for empowering me to take on this career path. Hence, I would like to dedicate this thesis to my grandparents, Nandita Mukherjee and Kartik Mukherjee for the love and inspiration they have always given me.

# TABLE OF CONTENTS

<b>ACKNOWLEDGEMENTS.....</b>	<b>iv</b>
<b>LIST OF TABLES.....</b>	<b>ix</b>
<b>LIST OF FIGURES.....</b>	<b>x</b>
<b>LIST OF SYMBOLS AND ABBREVIATIONS.....</b>	<b>xii</b>
<b>SUMMARY.....</b>	<b>xiii</b>
<b>CHAPTER 1 Introduction.....</b>	<b>1</b>
<b>1.1 Problem Statement.....</b>	<b>1</b>
<b>1.2 Research Goals.....</b>	<b>3</b>
<b>1.3 Format of Thesis.....</b>	<b>4</b>
<b>CHAPTER 2 Background and Literature Review.....</b>	<b>5</b>
<b>2.1 Fast Disconnect Switches for Hybrid Circuit Breakers.....</b>	<b>5</b>
<b>2.2 Piezoelectric Actuators.....</b>	<b>7</b>
2.2.1 Characteristics and limits of piezoelectric materials.....	7
2.2.2 Piezoelectric actuators for FMS.....	13
<b>2.3 Review of Control Methods for Piezo Actuators.....</b>	<b>17</b>
<b>2.4 Control of Individual Stacks of Piezo Actuators.....</b>	<b>19</b>
2.4.1 Relationship between mass, resonance frequency, and minimum switching time of a piezoelectric stack.....	19
2.4.2 Structure of PA and difference between stacks.....	20

2.5	Chapter Summary.....	21
<b>CHAPTER 3</b>	<b>Modeling of the PPA40L Actuator.....</b>	<b>22</b>
3.1	Identifying Stacks of the PPA40L Actuator.....	22
3.2	Digital Model Building.....	22
3.3	Model Verification.....	24
3.4	Chapter Summary.....	26
<b>CHAPTER 4</b>	<b>Individual Stack Control Methods.....</b>	<b>28</b>
4.1	Sequential Triggering Method.....	28
4.2	Input Shaping Method.....	31
4.3	Chapter Summary.....	33
<b>CHAPTER 5</b>	<b>Experimental Implementation of Control Methods.....</b>	<b>35</b>
5.1	Experimental Setup.....	35
5.1.1	Setup for driving piezo actuator.....	35
5.2	Experimental Displacement Curve when each Stack is Individually Triggered.....	40
5.3	Experimental Results and Discussion.....	43
5.3.1	Effect of varying $dv/dt$ of lower stack (Method 1).....	43
5.3.2	Effect of sequential triggering (Method 2).....	44
5.3.3	Effect of combining method 1 and method 2.....	46
5.4	Chapter Summary.....	47
<b>CHAPTER 6</b>	<b>Conclusion and Future Work.....</b>	<b>48</b>
6.1	Conclusion.....	48

<b>6.2</b>	<b>Future Work.....</b>	<b>49</b>
	<b>APPENDIX A. Terms used to describe piezoelectric actuator.....</b>	<b>51</b>
	<b>REFERENCES.....</b>	<b>52</b>

## LIST OF TABLES

Table 2-1: Description of symbols in equation 2.1 and 2.2 [3].	11
Table 2-2: Datasheet information of PPA40L actuator [17] used in this study.	16
Table 3-1: Individual stack parameters used in the digital model.	24
Table 5-1: Experimental Data Table for Undershoot (%) for Method 1.	44
Table 5-2: Experimental Data Table for Switching Time (10-90% of steady-state) (us) for Method 1.	44
Table 5-3: Experimental Data Table for Overshoot (%) for Method 2.	45
Table 5-4: Experimental Data Table for Switching Time (10-90% of steady-state) ( $\mu$ s) for Method 2.	46

## LIST OF FIGURES

Figure 2-1:	Circuit diagram of the Hybrid Circuit Breaker (HCB) topology proposed in [5].	7
Figure 2-2:	(a) Process of polarization of a piezoelectric ceramic crystal [8]; (b) Crystal structure of a piezoelectric ceramic [8].	8
Figure 2-3:	Generator and motor actions of a piezoelectric crystal [8].	10
Figure 2-4:	Effects of electric field (E) on polarization (P) and corresponding strain of a ceramic element [8].	10
Figure 2-5:	Impedance of piezoelectric ceramic as a function of frequency [8].	12
Figure 2-6:	Force per voltage response of Cedrat <sup>®</sup> APA30uXS actuator using COMPACT L. P. Model.	13
Figure 2-7:	(a) System view of the vacuum-interrupted PA-FMS prototype with Cedrat <sup>®</sup> APA1000XL actuator [15] proposed in [14] ; (b) Supercritical fluid-insulated PA-FMS prototype with Cedrat <sup>®</sup> PPA120XL actuator [16] shown in [1].	14
Figure 2-8:	(a) Cedrat <sup>®</sup> PPA40L actuator assembly [17]; (b) TOKIN <sup>®</sup> AE1010D16 piezo actuator stack [18].	15
Figure 2-9:	Typical displacement vs force characteristic of an actuator with the blocking force $F_{\text{block}}$ and stroke $\Delta L_{\text{fs}}$ marked [28].	16
Figure 2-10:	Displacement vs. Voltage curve from factory verification sheet of PPA40L actuator [19].	17
Figure 2-11:	Schematic of piezoelectric actuator used in the FMS along with the moving contact mass.	19
Figure 3-1:	MATLAB Simulink model of PPA40L piezo actuator with individual stacks and driving circuits modeled.	23
Figure 3-2:	Simulated displacement travel curves with varying contact mass compared to experimental travel curves.	25
Figure 4-1:	Schematic of experimental circuit to drive individual stacks of the PA.	28

Figure 4-2:	Time-shifted pulse for Sequential Triggering Method from the Tektronix AFG31022 Arbitrary Function Generator.	31
Figure 4-3:	Experimental curves for the PPA40L actuator provided in [3] showing how oscillations increase with an increase in both mass and $dv/dt$ of the input signal.	33
Figure 5-1:	Experimental test setup.	35
Figure 5-2:	PPA40L actuator with individual leads for each stack (left), PPA40L actuator [17] with positive leads connected and negative leads connected as received from the manufacturer (right).	36
Figure 5-3:	Amplified waveforms from 2 channels of the function generator measured across capacitor loads.	37
Figure 5-4:	(a) AE Techron <sup>®</sup> 7224 Power Amplifier (b) AE Techron 8524 <sup>®</sup> Power Amplifier.	38
Figure 5-5:	(a) Displacement sensor driver Lion Precision <sup>®</sup> ECL101 (b) Displacement sensor U5 probe positioned over a 1 g copper shim target on top of the PPA40L actuator (c) Payload masses designed to emulate contact weights of a circuit breaker.	39
Figure 5-6:	Displacement Sensor output in the compression region when each stack is individually triggered.	40
Figure 5-7:	Illustrations of fall time (or tail time $t_{tail}$ ) and switching time $t_{sw}$ as defined in [3]	42
Figure 5-8:	Experimental displacement curves plotted on MATLAB for better clarity of overshoot/undershoot region.	42
Figure 5-9:	Experimental displacement travel curves to illustrate the impact of varying $dv/dt$ of the lower stack.	43
Figure 5-10:	Experimental displacement travel curves to illustrate the impact of varying delay between stack actuation.	45
Figure 5-11:	Experimental displacement travel curves to compare the impact of method 1 (red), method 2 (yellow) and combination of methods 1 and 2 (violet).	47
Figure A-1:	Diagram showing components of the piezoelectric actuator and the terminology used to refer to them in this thesis.	51

## **LIST OF SYMBOLS AND ABBREVIATIONS**

AC	Alternating current
CB	Circuit breaker
DC	Direct current
DCCB	Direct-current circuit breaker
DER	Distributed energy resources
EDISON	Efficient DC Interrupter with Surge Protection
FMS	Fast mechanical switch
HCB	Hybrid circuit breaker
MVDC	Medium-voltage direct current
PA	Piezoelectric actuator
PZT	Lead-zirconate-titanate
SSCB	Solid-state circuit breaker

## SUMMARY

Hybrid circuit breakers (HCBs) are a potential protection solution for medium-voltage direct current (MVDC) power systems (1 kV – 100 kV). These HCBs require fast mechanical switches (FMS) with efficient actuators. Using piezoelectric actuators in an FMS has been a topic of discussion in previous works. Piezoelectric actuators are expected to enable fast, reliable, and controllable actuation for HCBs. During the HCB contact separation, higher oscillations will bring the contacts closer and reduce the voltage withstand capability of the HCB. Hence, both achieving a small actuation time and reduced overshoot in the displacement curve is necessary to ensure that the circuit breaker does not have to dissipate a large amount of energy and to reduce the probability of restriking. In order to accelerate the actuation, if the driving voltage of the piezo rises too fast, resonance may occur leading to increased oscillations and overshoot. This thesis aims to explore control mechanisms that would provide an acceptable trade-off between fast actuation and reduced oscillations by studying how individual piezoelectric stacks of an actuator can be controlled. Two control methods namely – sequential triggering method and input shaping method are presented. A digital simulation model is also built and validated. The two control methods are also experimentally tested and the results are analyzed. These control methods, when applied individually, show improved undershoot and overshoot characteristics in the displacement travel curve of the actuator. When the two control methods are combined and applied, the response is shown to be critically damped with a switching time of 426  $\mu$ s which is highly desirable for HCB application.

# CHAPTER 1 INTRODUCTION

## 1.1 Problem Statement

A piezoelectric actuator can be used as the driving mechanism to move contacts in fast disconnect switches such as those needed for hybrid DC circuit breakers [1].

A piezoelectric actuator will ideally generate a linear displacement under an applied electric field. An electronic circuit, consisting of a signal generator and an amplifier, can control this actuation. The amplifier itself can be fed by a capacitor bank since there is no need to provide a continuous current (or power). These characteristics make a piezoelectric actuator attractive for switchgear since they minimize steady-state power consumption. Furthermore, they are characterized by a fast mechanical response, typically in the order of tens to hundreds of microseconds for a complete actuation cycle.

From a control's perspective, such actuators behave like coupled resonance circuits [2]: The electrostatic capacitance of the device and the inductive loop with the lead wires and the circuit form an electrical resonance circuit, while the spring constant of the actuator and the moving mass form a mechanical resonance circuit. If not carefully damped electrically and mechanically, such an arrangement can lead to oscillations or large overshoots when driven fast. These challenges can be addressed by one of the following three methods:

1. Closed-loop feedback control based on measurement of mechanical properties (typically displacement or strain) [3].

2. Closed-loop feedback control based on measurement of electrical properties (typically voltage and current) [4].
3. Open-loop control based on careful signal shaping, which has been derived from numerical models.

Most piezoelectric ceramic materials only allow for a displacement on the order of 0.1%. Piezoelectric actuators exhibit a large aspect ratio with the dimension along the axis of displacement being significantly greater than the dimension in the other two space axes. For practical reasons, this is often achieved by stacking multiple ceramic units. While each of them is mechanically in series, their electric circuits are often connected in parallel. This leads to one more degree of freedom to optimize the total displacement: The units could potentially each be driven independently, allowing to optimize each charging characteristic to take into account the position in the stack.

When used for the application of medium voltage hybrid DC circuit breakers such as the EDISON (Efficient DC Interrupter with Surge Protection) project [1], both achieving a small actuation time and reduced overshoot in the displacement curve is necessary to ensure that the circuit breaker does not have to dissipate a large amount of energy and to reduce the probability of restriking. This work explores control mechanisms that would enable us to find an optimum level of these two parameters by studying how individually stacked ceramics of a parallel prestressed stacked actuator can be controlled. The reason to pursue this individual control method is that during the actuation process, each stack is exposed to different mechanical conditions due to their different positions in the stack. For example, while the stack is contracting during the actuator opening process, the lower unit would be oscillating with higher mass than the upper units due to the greater moving mass

vertically above it. This is an interesting aspect that may indicate that using the same driving signal for all individual stacks may not be the most optimal method for fast actuation. The proposed study aims to conduct a literature review of the existing work done in this area, explore digital modeling approaches for the control of individual stacks of a PA, and present experimental results of various individual control mechanisms.

## **1.2 Research Goals**

The objective of this research is to study methods to individually control stacks of a piezoelectric actuator for fast mechanical switches with the aim of improving its displacement travel curve by reducing oscillations in the response. The specific objectives can be summarized as:

1. Conducting a detailed literature review on hybrid circuit breakers, fast mechanical switches, and existing methods to control them.
2. Studying two methods to control individual stacks of a piezoelectric actuator for fast mechanical switches, namely – sequential triggering method and input shaping method.
3. Building a digital simulation model of the piezoelectric actuator and setup used to test these methods to better understand the dynamics of the system.
4. Validating the accuracy of the digital simulation model of the system.
5. Experimentally implementing these two individual control methods as well as a combination of the two methods.
6. Analyzing the benefits of these control methods as well as suggesting further improvements and next steps for this research work.

### 1.3 Format of Thesis

The format of this thesis is as follows:

1. Chapter 2 reviews the existing literature on hybrid circuit breakers, fast mechanical switches, characteristics of piezoelectric actuators, and control methods for them. It also describes the hypothesis behind proposing to control individual stacks of a piezoelectric actuator to obtain an improved displacement travel curve.
2. Chapter 3 aims to identify the parameters of the stacks of the piezoelectric actuator used for this study and describes the simulation model of the setup used to implement the control methods proposed in this study. It also verifies the accuracy of the model by comparing simulation results with experimental results under similar test conditions.
3. Chapter 4 describes the theory of two open-loop control methods to control individual stacks of a piezoelectric actuator.
4. Chapter 5 focuses on the experimental implementation of these control methods. It describes the experimental setup and results as well as the conclusions from the results.
5. Chapter 6 summarizes the conclusions and contributions of this research work.

## **CHAPTER 2      BACKGROUND AND LITERATURE REVIEW**

This chapter reviews existing literature on hybrid circuit breakers, fast mechanical switches, and the characteristics and control of piezoelectric actuators. It also introduces the hypothesis for the control of individual stacks of a piezoelectric actuator to improve the displacement response during actuation.

### **2.1    Fast Disconnect Switches for Hybrid Circuit Breakers**

The advent and development of new energy technologies such as distributed energy resources (DERs), electric vehicles, and energy storage units call for more research in the field of direct-current (DC) power systems. While high-voltage and low-voltage DC systems are already popular for power transmission and industrial use, respectively, medium-voltage direct-current (MVDC) systems (1 kV – 100 kV) are still developing. MVDC systems will likely find applications in DC microgrids, DC shipboard power systems, DC railway systems, and DC wind collector systems [5]. In addition, there is a possibility that MVDC will also find use in DC fast charging of large electric vehicles. Hence, developing reliable switchgear for these systems is an important topic of research and a relatively unexplored field.

The primary challenge in developing circuit breakers (CBs) for DC systems as opposed to alternating-current (AC) systems is the absence of a natural zero crossing of the DC current i.e. the point where the current alternates and begins to change direction. This has led to the development of direct-current circuit breaker (DCCB) technologies that artificially induce a zero crossing. Solid-state circuit breakers (SSCB) and hybrid circuit

breakers (HCB) are two such solutions where an artificial zero crossing is induced during a fault when current is commutated from the normal conduction path to the energy absorption path. SSCBs are circuit breakers composed purely of solid-state devices (power semiconductors). They are capable of interrupting fault currents within a few microseconds or less [6], [7]. However, one of the most significant challenges associated with SSCBs is high ON-state losses leading to overheating, damage, or early aging of semiconductor devices [7] unless properly cooled. The large cooling systems lead to low power density and low efficiency. To minimize this problem, HCB technologies were proposed where the normal conduction path consists of a mechanical switch with reduced ON-state losses owing to a very minimum conduction state resistance in the order of micro-ohms [3]. One such HCB technology proposed in [5] is shown in Figure 2-1. The normal conduction path has a mechanical disconnecter type switch or a fast mechanical switch (FMS). The parallel commutation branch consists of the fault current commutation circuit (FC3) and surge arrestors to absorb the fault energy.

Replacing solid-state switches with a mechanical switch in the normal conduction path comes with the drawback of reduced switching speed due to the mechanical inertia of the contacts. As shown in [3], if the switching time increases from 0.1 ms to 1 ms the circuit breaker needs to interrupt 10 times the peak current and 100 times the peak energy for a standard 12 kV DC system. Hence, it is crucial to reduce the switching time of the FMS through optimal control strategies. Faster switching of the FMS is also going to be accompanied by greater mechanical oscillations, which could reduce the voltage withstand capability of the circuit breaker and increase the risk of restriking. Hence, a trade-off would be required between these two parameters.

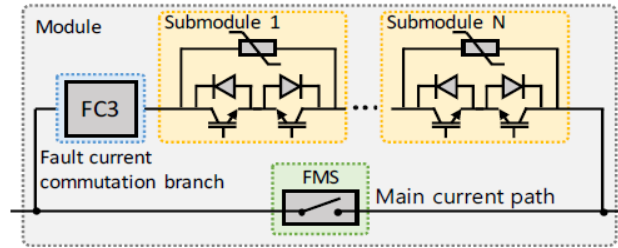


Figure 2-1: Circuit diagram of the Hybrid Circuit Breaker (HCB) topology proposed in [5].

## 2.2 Piezoelectric Actuators

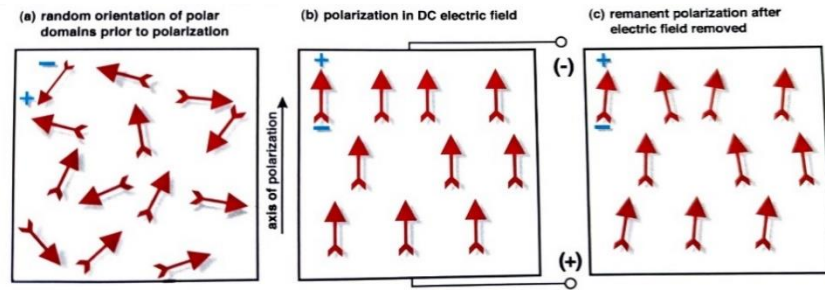
### 2.2.1 Characteristics and limits of piezoelectric materials

#### 2.2.1.1 Piezoelectricity in Ceramics

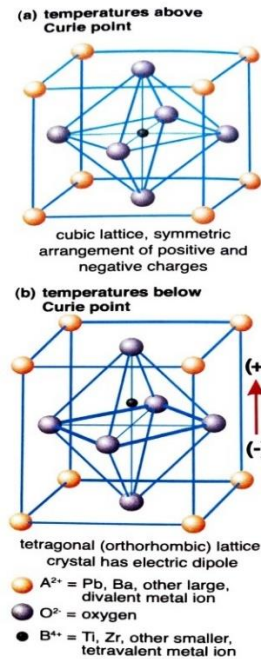
A wide variety of ceramics exhibit piezoelectric properties. This may be problematic for certain applications such as semiconductors and capacitors. However, certain types of ceramics with especially pronounced piezoelectric properties are used for actuators. These have a wide variety of applications such as in motors, precise position control and generating sonic and ultrasonic signals [8]. They exhibit the property of piezoelectricity i.e., a linear electrical polarization when subjected to mechanical force or a linear strain under applied field. Lead-zirconate-titanate (PZT) materials are one of the most commonly used piezoelectric materials owing to their greater sensitivity and higher operating temperatures [8]. As shown in Figure 2-2(b), piezoelectric ceramics have a perovskite crystal structure and below a critical temperature known as the Curie point, each crystal has a tetragonal or rhombohedral symmetry with a dipole moment.

To make a piezoelectric ceramic, the metal oxide powders are pressed and molded into the desired shape and fired at a particular temperature giving it a crystalline structure.

PZT-based materials are also ferroelectric and the electric dipoles must be aligned before use. Once electrodes are applied to the crystal surfaces, they are poled by placing them in a DC electric field at a temperature below the Curie temperature [8]. As shown in Figure 2-2(b), this polarization causes a majority of the polar domains in the crystal to align along



(a)



(b)

Figure 2-2: (a) Process of polarization of a piezoelectric ceramic crystal [8]; (b) Crystal structure of a piezoelectric ceramic [8].

the applied electric field. Most of these dipoles remain aligned even after the removal of the electric field and this gives the crystal a permanent polarization. The application of tension and compression on a polarized piezoelectric ceramic leads to the generation of voltages with opposite polarity and proportional to the magnitude of the force. A compressive force along the direction of polarization generates a voltage of the same polarity as the polarizing voltage and a tensile force along the direction of polarization generates a voltage opposite to that of the polarizing voltage. Similarly, applying an electric field to such crystals results in dimensional changes according to the field strength and polarity. These effects are known as the direct piezoelectric effect and converse piezoelectric effect, respectively [8]. They can also be interpreted as the generator and motor actions of piezoelectric crystals as depicted in Figure 2-3.

Similar to ferromagnetic materials, piezoelectric crystals are ferroelectric and exhibit hysteresis as shown in Figure 2-4. This is an undesirable effect that leads to large errors when piezoelectric actuators are used in positioning applications [9]. The constitutive equations describing linear piezoelectricity as stated in the 1976-1987 IEEE standard [10] is:

$$D_m = \varepsilon_{mn}^T E_n + d_{mkl} T_k \quad (2.1)$$

$$S_{ij} = d_{ijn} E_n + s_{ijkl}^E T_{kl} \quad (2.2)$$

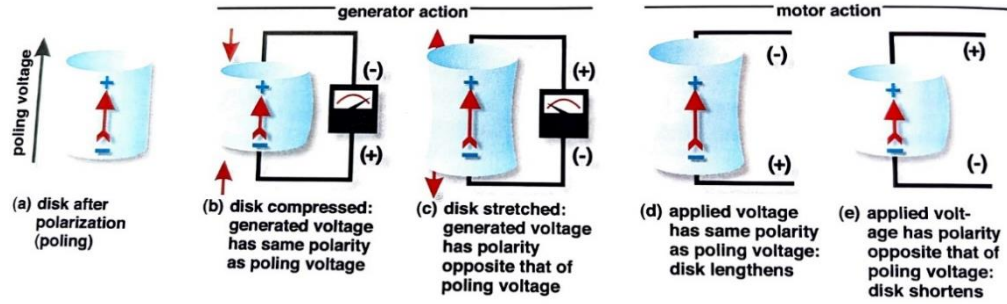


Figure 2-3: Generator and motor actions of a piezoelectric crystal [8].

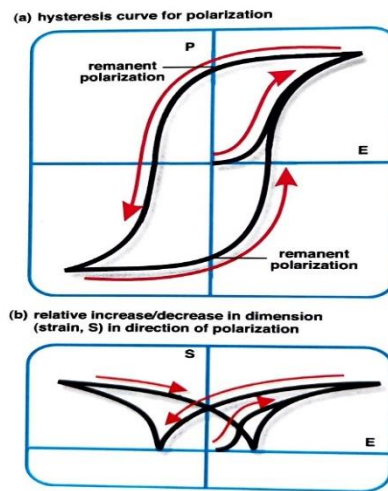


Figure 2-4: Effects of electric field (E) on polarization (P) and corresponding strain of a ceramic element [8].

Table 2-1 describes the notations used in the above equations in detail. The electric field vectors  $\vec{D}, \vec{E}$  have three components along the  $x, y,$  and  $z$  directions while the mechanical field vectors  $\vec{T}, \vec{S}$  contain six components – three of them normal components and three rotational components. The piezoelectric actuator (PA) used in this study is exposed only to a normal electric field, which produces stress along the same axis. It also operates in longitudinal mode and hence the rotational components can be neglected. Under these conditions, the above equations modify to [3]:

$$D_3 = \varepsilon_{33}^T E_3 + d_{33} T_3 \quad (2.3)$$

$$S_3 = d_{33} E_3 + s_{33}^T T_3 \quad (2.4)$$

The subscript 33 indicates that both the input voltage and the generated stress are along the z-axis.

Table 2-1: Description of symbols in equation 2.1 and 2.2 [3].

Notation	Description	Unit
$D_m$	Electric flux density; vector	$C^* m^{-2}$
$E_n$	Electric field intensity	$V^* m^{-1}$
$S_{ij}$	Mechanical strain; tensor rank 2	-
$T_{kl}$	Mechanical stress; tensor rank 2	$N^* m^{-2}$
$\varepsilon_{mn}^T$	Electric permittivity; tensor rank 2	$F^* m^{-1}$
$d_{mkl}, d_{ijn}$	Piezoelectric strain constants; tensor rank 3	$C^* N^{-1}; mV^{-1}$
$s_{ijkl}^E$	Elastic compliance constants; tensor rank 4	$m^{2*} N^{-1}$

#### 2.2.1.2 Limits of piezoelectric actuators

Due to their electromechanical coupling nature, resonance, and anti-resonance points are observed on the impedance curve of piezoelectric ceramics as depicted in Figure 2-5. The resonance frequency is a unique frequency for each piezoelectric ceramic element at which it vibrates most readily in response to an electrical input [8]. It depends on the composition, volume, and shape of the element. In the resonance region, these rapid vibrations give rise to high mechanical stress, which may damage the ceramic material primarily due to its sensitivity to tensile forces. Studies were conducted to observe

the voltage and force limits due to this high stress generated during actuation in the resonance region by Cedrat<sup>®</sup> Technologies using a Lump Parameter (LP) model implemented on Microsoft Excel [11]. This model named COMPACT is available as a publicly released freeware. Figure 2-6 shows the force per voltage response of the APA30 $\mu$ XS actuator [12] using the COMPACT model. It was observed that the resonance region amplifies the dynamic forces to 0.5 N/V which means that the dynamic force at resonance would reach 37.5 N for a full-scale actuation of 75 V. Such a force would likely damage the actuator [12]. Hence, operating at the resonance region would result in the fastest actuation but the actuation voltage would have to be reduced due to the mechanical stress limits. To improve this material limitation, a prestress or a preload is applied to most commercially available actuators to maintain its piezoelectric ceramic in compression and counteract any possible harmful tensile forces during actuation.

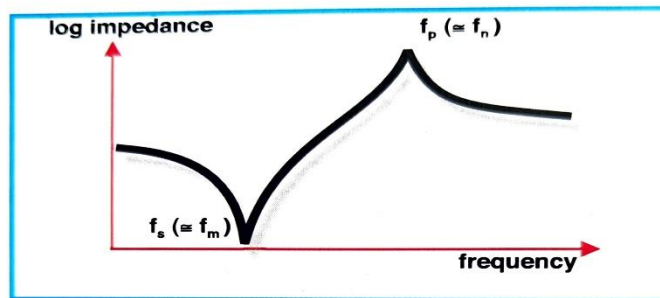


Figure 2-5: Impedance of piezoelectric ceramic as a function of frequency [8].

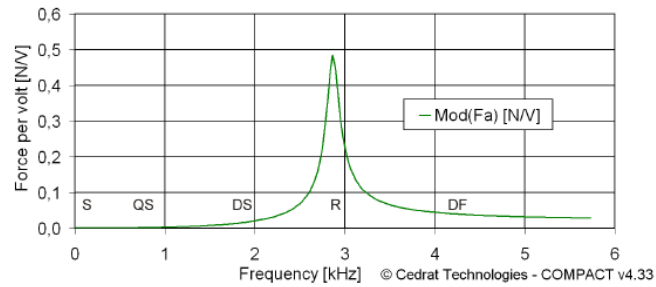


Figure 2-6: Force per voltage response of Cedrat® APA30uXS actuator using COMPACT L. P. Model.

### 2.2.2 Piezoelectric actuators for FMS

Various actuator technologies have been investigated for fast mechanical switches in HCBs [13]. For example, the Thomson coil actuator is an electromagnetic actuator capable of fast interruptions within 1 ms [13]. However, these types of actuators have two major drawbacks: limited controllability of the displacement travel curve and low driving efficiency [3]. Optimizing the displacement curve through control mechanisms is important for actuators used in disconnecter switches for circuit breakers, especially for the sequential insertion control scheme [5], as the exact gap distance and voltage withstand capability of the circuit breaker would directly be determined by this.

To mitigate these issues, a piezoelectrically actuated FMS (PA-FMS) has been proposed in [14], which can enable fast, reliable, and controllable actuation for HCB applications. The deformation of the piezoelectric ceramics during actuation is directly transferred to the moving contacts of the HCB allowing the PA-FMS to be fast and compact. Piezoelectric actuators are characterized by high actuation efficiency and controllability of the displacement travel curve. Some of these control methods have been

reviewed in Section 2.3. Figure 2-7(a) provides a system view of the PA-FMS technology proposed in [14]. The switch paddle consisting of the Cedrat<sup>®</sup> APA1000XL actuator [15] and the FMS contacts is placed inside a vacuum chamber. The paddle can be switched on or off by providing an input driving voltage signal to the piezo actuator. A switch opening time of 1.4 ms and a breakdown voltage of over 20 kV was achieved with this prototype. A modified and more optimized design of the PA-FMS in Figure 2-7(b) with supercritical fluid insulation and reduced contact resistance achieved a significantly reduced switching time of 300  $\mu$ s with a 260 g contact.

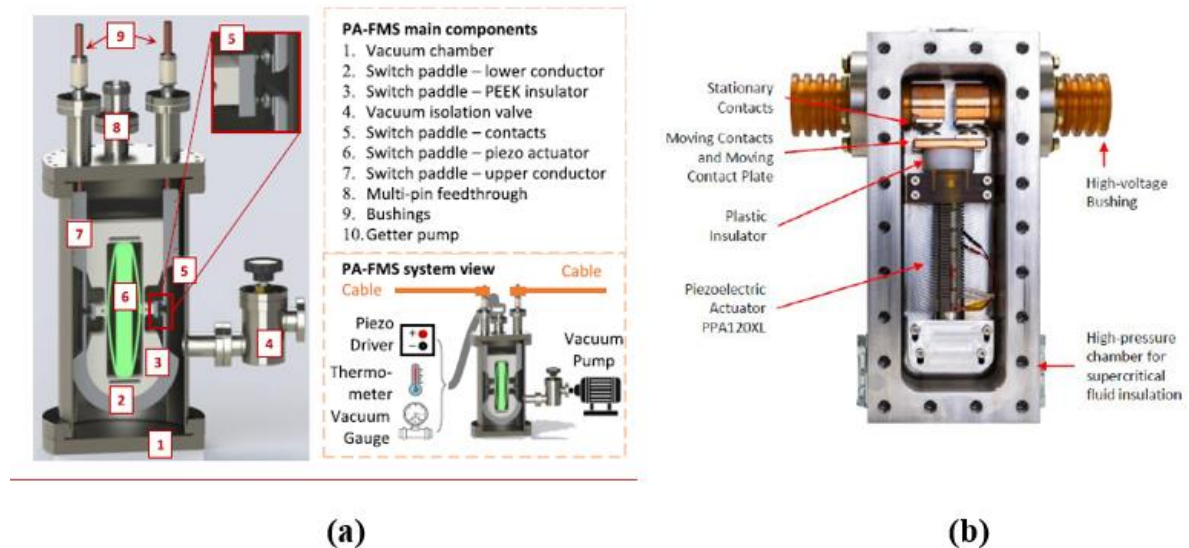


Figure 2-7: (a) System view of the vacuum-interrupted PA-FMS prototype with Cedrat<sup>®</sup> APA1000XL actuator [15] proposed in [14] ; (b) Supercritical fluid-insulated PA-FMS prototype with Cedrat<sup>®</sup> PPA120XL actuator [16] shown in [1].

For this study, the Cedrat<sup>®</sup> PPA40L actuator [17] is used to conduct experiments to understand the impact of individual stack control of a piezoelectric actuator. As shown in Figure 2-8(a), it consists of two multi-layered piezo actuator stacks protected against tensile forces by a prestressing external stainless steel spring frame. Information regarding the

exact specification of each individual stack in this actuator has not been made available by the manufacturer. To estimate this, the actuator parameters in [17] were compared to standard available piezo stacks in the market. The parameters of TOKIN<sup>®</sup>-KEMET<sup>®</sup>'s AE1010D16DF-Thin Coating [18] shown in Figure 2-8(b) was found to be very close to the available values.

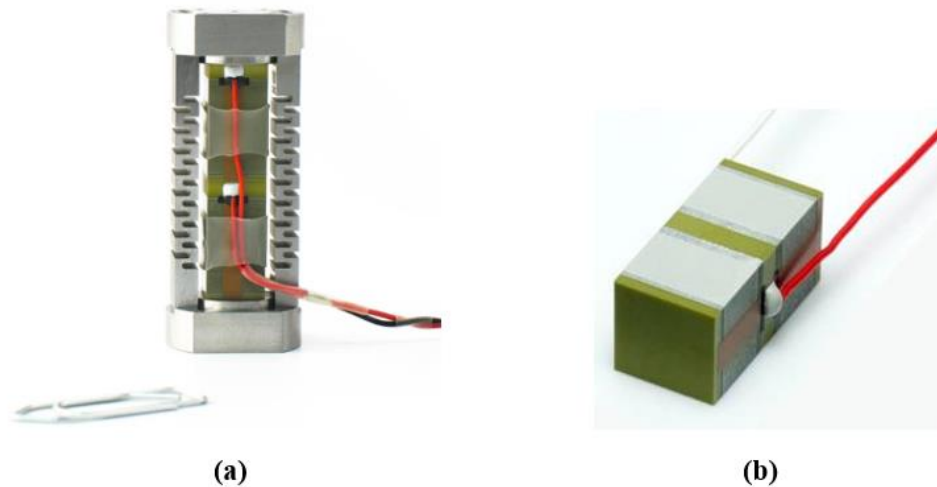


Figure 2-8: (a) Cedrat<sup>®</sup> PPA40L actuator assembly [17]; (b) TOKIN<sup>®</sup> AE1010D16 piezo actuator stack [18].

Table 2-2 provides detailed information regarding the parameters of the PPA40L actuator. It is characterized by a nominal stroke of 44  $\mu\text{m}$  and a significant blocking force of 3500 N. The blocking force of a piezo actuator is the maximum force that can be generated by it. It can be achieved when the displacement is completely blocked during actuation by an infinitely stiff load. The blocking force and stroke of an actuator is marked in the displacement vs force characteristics shown in Figure 2-9. The displacement versus voltage characteristics of the PPA40L actuator is shown in Figure 2-10. For the EDISON FMS, the PPA120XL actuator [16] is used which has a much higher stroke of 130  $\mu\text{m}$  and

a blocking force of 7000 N. However, for the purpose of the tests in this study, the smaller PPA40L actuator is used to avoid potential damage to the valuable PPA120XL actuator.

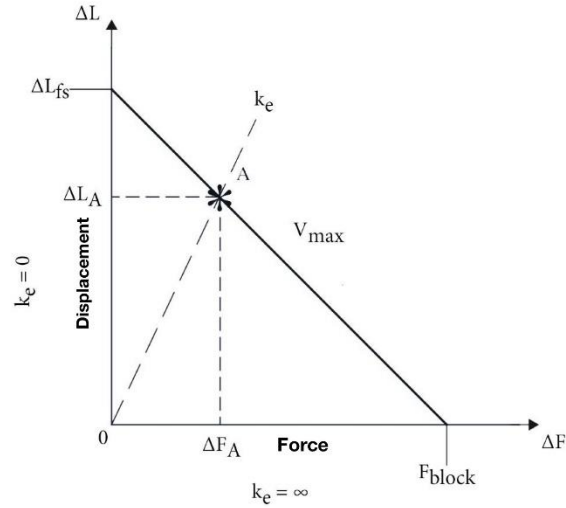


Figure 2-9: Typical displacement vs force characteristic of an actuator with the blocking force  $F_{block}$  and stroke  $\Delta L_{fs}$  marked [28].

Table 2-2: Datasheet information of PPA40L actuator [17] used in this study.

Parameter of PPA40L	Value
Nominal Stroke	44 $\mu\text{m}$
Blocked Force	3500 N
Stiffness	110 N/ $\mu\text{m}$
Resonance frequency (blocked-free)	8.3 kHz
Voltage Range	-20 to +150 V
Mass	92 g
Capacitance	8.8 $\mu\text{F}$

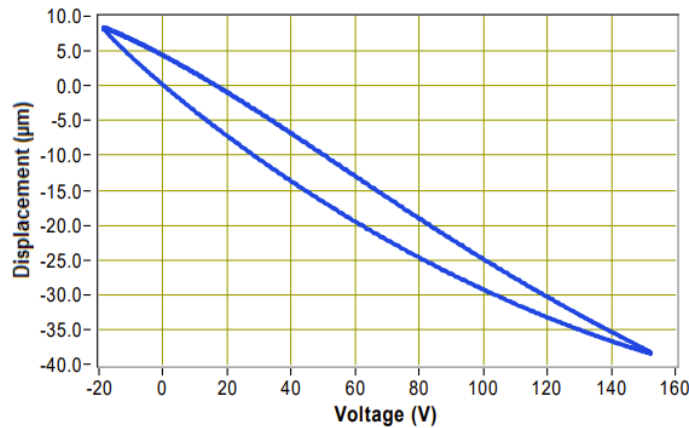


Figure 2-10: Displacement vs. Voltage curve from factory verification sheet of PPA40L actuator [19].

### 2.3 Review of Control Methods for Piezo Actuators

This section summarizes the most significant papers on the control of piezo actuators. The concept of individual stack control of a piezo actuator by sequentially triggering each stack has been explored in [20]. This work uses a MOSFET-based high-frequency driving circuit to generate time-delayed pulses to trigger each of the piezo stacks. The time delay is constant and calculated according to the stress wave theory. It is only a function of Young's modulus and the density of the piezoceramic material. Using that method provides a cumulative high-magnitude stress wave at the top of the final stack and a small rise time of the displacement curve of the piezo. However, the rise time of the driving pulses would have to be comparable to the time delay, which is approximately in the range of 8  $\mu\text{s}$  for our stack. This could potentially lead to unacceptable overshoots and damage to the ceramic material. Additionally, the characteristics of the driving pulses are restricted by the MOSFET's characteristics. Paper [4], [21] discusses the benefit of controlling the displacement curve of a piezo actuator by the amount of current fed into it using

feedforward compensation and a PID controller. This method greatly improves non-linear effects such as hysteresis and drift and hence has better results for positioning applications. The input-shaping method to control a piezo actuator has been studied in [21]. Fourier transform was used to generate input waveforms to compensate for the non-linear dynamics of the actuator. However, this analysis was done only for applications with periodic input signals and primarily focused on improving tracking errors. A review of different driving methods for piezo actuators for discussed in [9]. The advantages and disadvantages of the voltage-driven method, charge-driven method, and capacitor insertion method were analyzed. The voltage-driven method is characterized by its simplicity but cannot address the non-linear effects such as hysteresis and creep. The charge-driven method can address these non-linearities but requires significantly complex equipment. The capacitor insertion method is a comparatively economical method to reduce non-linear effects. However, it limits the operating range of the actuator. The research work in [22] conducts a similar review on driving methods for these actuators and the conclusions agree with [9]. A method for critical damping of the travel curve of a piezo actuator is studied and analyzed in [23]. This work models the actuator system according to the Goldfarb model in [2] and applies various filtering techniques to reduce the vibrations in a piezo actuator for DC circuit breaker applications. This is done through closed-loop control, which is a promising technique but of significant complexity. Research on the aspect of individually controlling each stack of the piezo actuator is hence limited and is required to be explored.

## 2.4 Control of Individual Stacks of Piezo Actuators

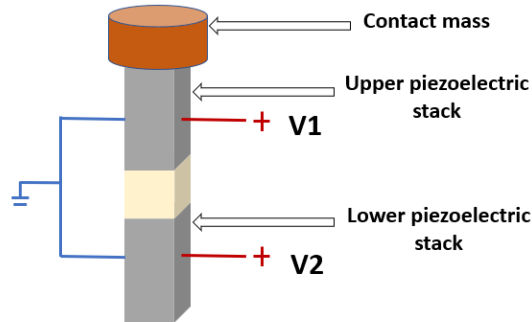


Figure 2-11: Schematic of piezoelectric actuator used in the FMS along with the moving contact mass.

### 2.4.1 Relationship between mass, resonance frequency, and minimum switching time of a piezoelectric stack

During the actuation process, the nature of the response and the displacement travel curve of the piezoelectric actuator is affected by its resonance frequency [1]. The closer a vibrating body is operated to its resonance frequency, the higher the mechanical vibrations. The resonance frequency is related to the mass of the PA as well as the mass of the load according to the equation:

$$f_r = \frac{1}{2\pi} \sqrt{\frac{K_{PA}}{m_{PA} + m_{load}}} \quad (2.5)$$

where  $f_r$  is the resonance frequency of the PA,  $K_{PA}$  is the stiffness of the PA,  $m_{PA}$  is the mass of the PA and  $m_{load}$  is the mass of the load or the moving contacts on top of the PA. The fastest switching time of a PA is related to this resonance frequency as  $t_{SW} = 1/3 f_r$  [1]. Since Equation 2.5 is derived from the relationship between the resonance frequency and

mass of any mechanically oscillating object, it should be valid for each individual stack in the PA as well.

#### *2.4.2 Structure of PA and difference between stacks*

Figure 2-11 illustrates the internal mechanical structure of the piezoelectric actuators used in experiments for this thesis. It consists of two vertically stacked piezoelectric stacks and each stack has an insulating end plate that electrically separates it from the next stack above or below. During the actuation process, a voltage signal is applied across the electrical leads of each stack, which generates a deformative stress that elongates or compresses it. Traditionally, each stack of a multi-stack actuator is manufactured to receive the exact same input voltage signal. This is achieved by soldering all the positive leads together and all the negative leads together. However, if the movement of individual stacks are considered during the actuation process, each stack pushes along different masses owing to their different position in the actuator. The lower stack pushes the masses of the upper stack, moving contact, and pre-stressing structure along with its own mass. The upper stack pushes the masses of the moving contact, pre-stressed structure and its own mass, but not the lower stack since the two stacks are not mechanically connected. Instead, they are just mechanically stacked on top of each other. Hence, according to Equation 2.5, the two stacks will have different resonance frequencies owing to the different effective masses they are pushing during actuation. If actuated with the same voltage signal, the lower stack will be operating closer to its resonance frequency and hence have greater mechanical vibrations. Chapter 5, Section 2 validates this hypothesis through experimental results of each stack being triggered individually. The displacement curve for the lower stack has a higher percentage undershoot than the upper stack when triggered by the same

actuation voltage. Hence, the need to explore methods to control these stacks individually instead of providing identical actuation signals to each stack. Methods to improve the response of the actuator through control of individual stacks are discussed in Chapter 4.

## **2.5 Chapter Summary**

This chapter reviews literature regarding hybrid circuit breakers and piezoelectric actuators for fast mechanical switches. The characteristics and limits of piezoelectric materials such as non-linearities and dynamic force limits are studied. Existing methods for the control of piezoelectric actuators are reviewed and analyzed. Finally, the theory and hypothesis of the control of individual stack of a PA is presented.

## **CHAPTER 3      MODELING OF THE PPA40L ACTUATOR**

This chapter focuses on the digital model construction of the test setup to better understand the dynamics of the system. It aims to identify and model individual stacks of the PPA40L piezoelectric actuator as required by the control methods proposed in this work. The accuracy of this model is verified by comparing simulation results against experimental travel curves.

### **3.1 Identifying Stacks of the PPA40L Actuator**

This project studies the control of Cedrat<sup>®</sup> PPA40L piezo actuators, the technical specifications for which are given in [17]. However, information regarding the exact specification of each individual stack in this actuator has not been made available by the manufacturer. For this project, it is crucial to have an estimate of individual stack parameters as the digital modeling would require this information. To estimate this, the actuator parameters in [17] were compared to standard available piezo stacks in the market. The parameters of Tokin-Kemet's AE1010D16DF-Thin Coating [18] were found to be very close to the available values. The initial digital model of the actuator control system hence uses these values.

### **3.2 Digital Model Building**

Figure 3-1 illustrates the system used to model and study the PPA40L actuator using the Simulink modeling software. The blue side on the left is the electrical system components while the green side on the right is the mechanical system components. The

piezo stack block represents the electrical and force characteristics using the following linear equations:

$$S = s^E T + d' E \quad (3.1)$$

$$D = d T + \epsilon^T E \quad (3.2)$$

where  $S$  is the strain tensor,  $T$  is the stress tensor,  $E$  is the electric field vector,  $D$  is the electric displacement vector,  $s^E$  is the elastic compliance matrix when subjected to a constant electric field,  $d$  is the piezoelectric constant matrix,  $\epsilon^T$  is the permittivity measured at constant stress.

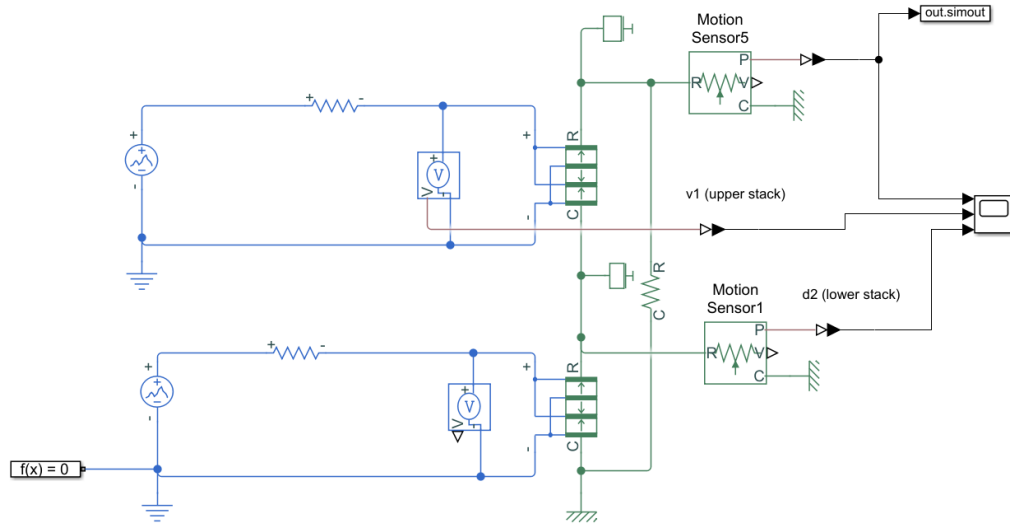


Figure 3-1: MATLAB Simulink model of PPA40L piezo actuator with individual stacks and driving circuits modeled.

The lower stack's mass is represented by the mass attached to the movable end of the lower stack. The mass attached to the movable end of the upper stack represents the upper stack's mass as well as that of the moving circuit breaker contact. The value of this mass can be

adjusted according to the mass of the contacts used. The spring connected across the two stacks represents the spring constant of the steel frame used for pre-stressing the actuator. Motion sensors are used to measure the displacement curve of the actuator. The electrical driving circuit for the individual stacks consists of a piecewise linear voltage source to model the post-amplification actuation voltage and a damping resistor. The stack parameters used are those of Tokin-Kemet's AE1010D16DF-Thin Coating [18] and are given in Table 3-1. The mechanical quality factor is estimated from Kemet's user manual [24]. The pre-stressing force itself cannot be modeled using this modeling software and hence slight inaccuracies in the response relating to this aspect are expected.

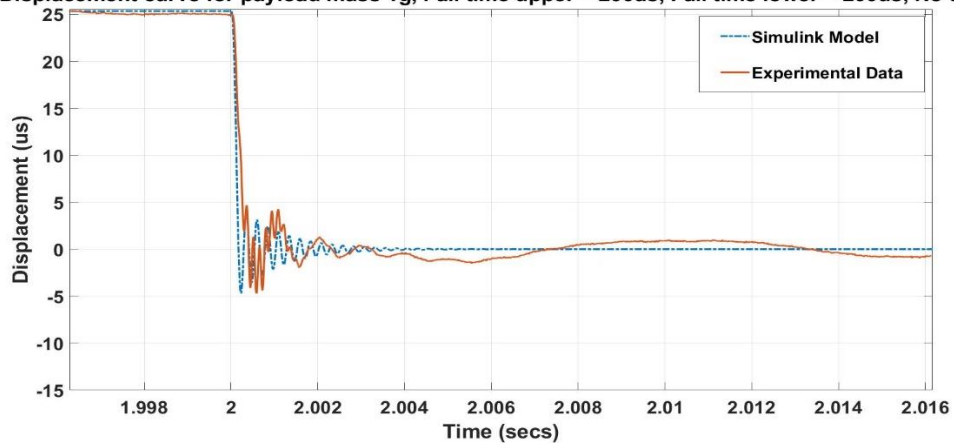
Table 3-1: Individual stack parameters used in the digital model.

Parameter of PPA40L Stacks Used in Digital Model	Value
Stack area	100 mm <sup>2</sup>
Stack length	20 mm
Test Voltage $V_0$	150 V
No-load displacement at $V_0$ volts	22 $\mu$ m
Capacitance	4.4 $\mu$ F
Resonance frequency	69 kHz
Mechanical quality factor	60

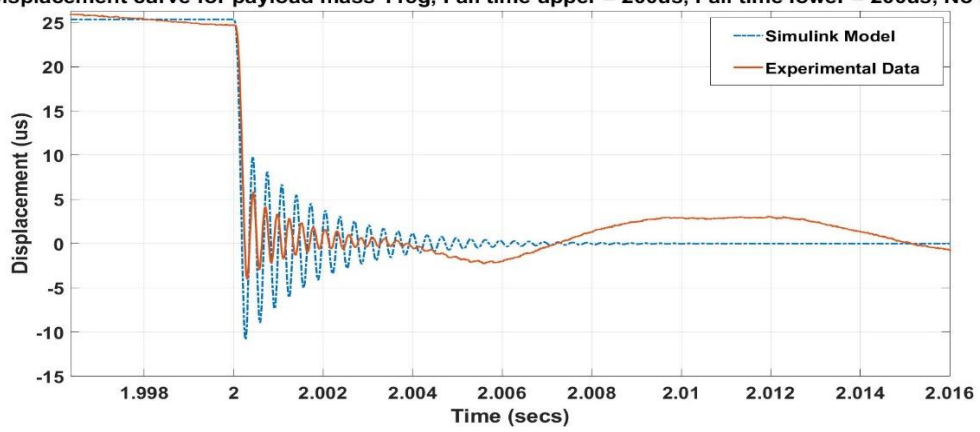
### 3.3 Model Verification

The digital model of the PPA40L actuator as described previously, is verified by comparing it to experimentally obtained displacement travel curves of the same tests. Figure 3-2 shows the comparison between simulated and experimental displacement travel

Displacement curve for payload mass 1g, Fall time upper = 200us, Fall time lower = 200us, No delay



Displacement curve for payload mass 115g, Fall time upper = 200us, Fall time lower = 200us, No delay



Displacement curve for payload mass 220g, Fall time upper = 200us, Fall time lower = 200us, No delay

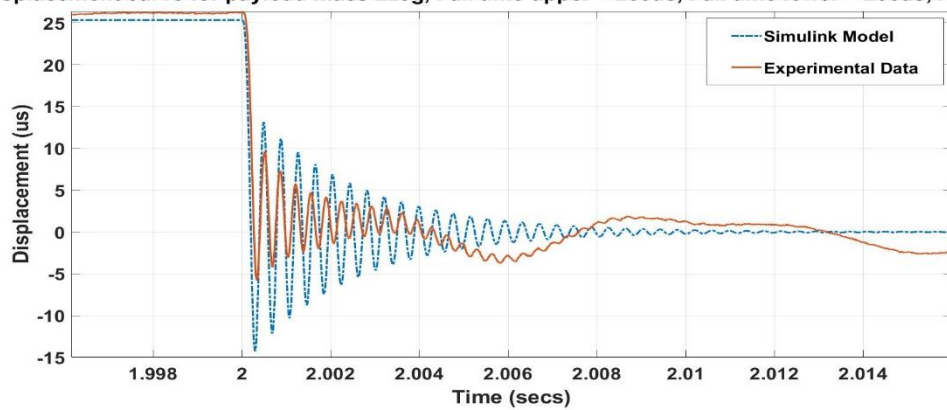


Figure 3-2: Simulated displacement travel curves with varying contact mass compared to experimental travel curves.

curves when each stack of the PPA40L actuator is triggered with a voltage of 95 V, fall time of 200  $\mu$ s, and varying contact masses. As expected, the oscillations in the response increase with an increase in contact mass. The digital model captures the falling edge and the frequency of initial oscillations well. There is a slight mismatch in the undershoot of the response. This can be attributed to the fact that the pre-stressing force has not been represented in the digital model. The overshoot of the experimental response is much lower than the simulated overshoot due to the actuator being restricted by compression constraints due to the pre-stressing frame [3]. In general, the undershoot region is represented better than the overshoot region, which is the more critical parameter for our application.

The digital model matches the initial high-amplitude and high-frequency oscillations due to the actuator's mechanical properties such as mass, spring constant, and damping. The low-amplitude and low-frequency oscillations seen in the experimental curves are considered to be externally introduced by the mechanical fixtures of the setup. These oscillations vary with the use of different kinds of setups [3]. Methods to reduce these external vibrations through feedback control are highlighted in [3]. This model can be used in further studies to understand the impact of different open-loop control methods for the PA system.

### **3.4 Chapter Summary**

This chapter presents a digital simulation model of the test system used for this research. The system aims to model the electrical and mechanical parameters of the

individual stacks of the PPA40L actuator as well as the driving system. The model building process is described and the simulation results are compared with experimental results. The falling edge and frequency of oscillation is captured well by the model. There is a slight error in the amplitude of oscillations due to the absence of a pre-stressing force in the digital model.

## CHAPTER 4 INDIVIDUAL STACK CONTROL METHODS

This chapter describes the theory of two methods that can be used to control individual stacks of a PA, namely- the sequential triggering method and the input shaping method. They are simple control methods that can be implemented through the experimental circuit shown in Figure 4-1.

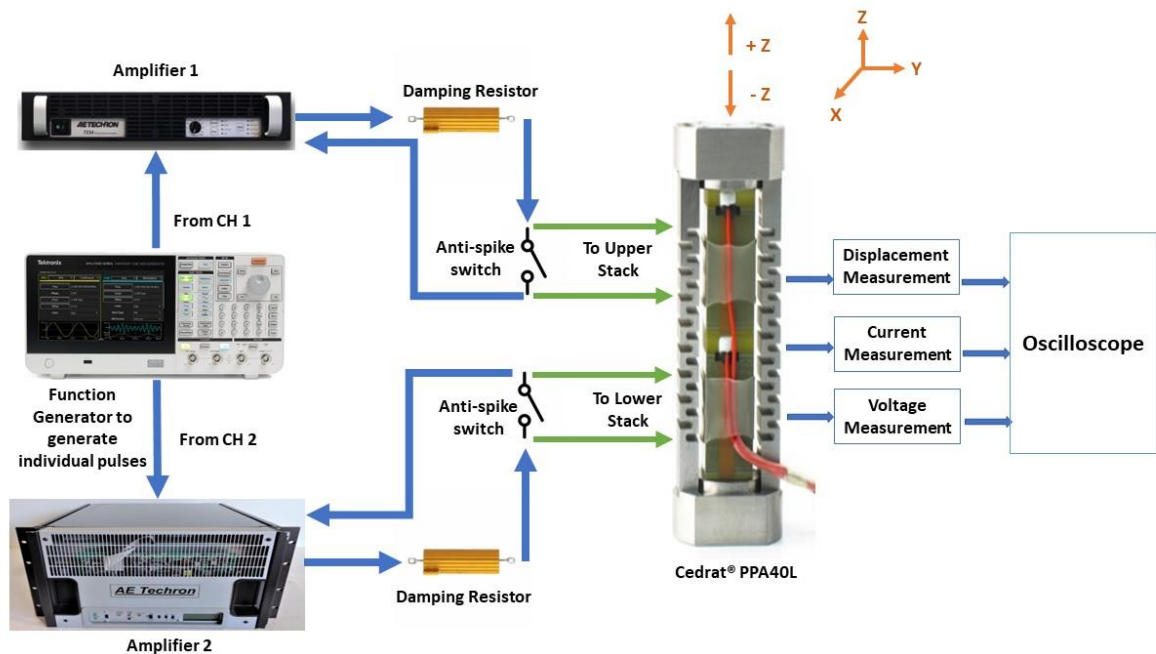


Figure 4-1: Schematic of experimental circuit to drive individual stacks of the PA.

### 4.1 Sequential Triggering Method

The method of sequentially triggering PA stacks by introducing a delay between the actuation of subsequent stacks has been introduced in [20]. This method utilizes the speed of propagation of the stress wave in the piezoelectric ceramic material and the height of each stack to calculate the propagation delay of the stress wave through each stack. An

optimal delay between the actuation of each stack could help in damping out the overall undershoot of the displacement curve of the PA.

Considering the ceramic material of the PA to be operating within its elastic limit during the actuation process, the mechanical stress  $T$  can be equated to the displacement of the actuator along the  $z$ -axis  $u(t,z)$  using Hooke's Law [20] as:

$$T = E \frac{\partial u(t, z)}{\partial z} \quad (4.1)$$

Where  $E$  is the Young's modulus of the ceramic material.

Also, applying Newton's second law for an infinitesimal volume element we get,

$$\frac{\partial T}{\partial z} = \rho \frac{\partial^2 u(t, z)}{\partial t^2} \quad (4.2)$$

Where  $\rho$  is the density of the ceramic material.

Combining Equations 4.1 and 4.2, the speed of propagation of the stress wave  $v$  can be obtained from,

$$\frac{\partial^2 u(t, z)}{\partial t^2} = v^2 \frac{\partial^2 u(t, z)}{\partial z^2} \quad (4.3)$$

$$v = \sqrt{E/\rho} \quad (4.4)$$

The density of the stacks of the PPA40L actuator as specified by the manufacturer is  $7930 \text{ kg/m}^3$  and the Young's modulus of the stack is  $4.4 \times 10^{10} \text{ N/m}^2$ . As per Equation 4.4, the velocity of propagation of the stress wave for the PPA40L stacks is  $2355 \text{ m/s}$ .

Taking the Laplace transform of Equation 4.3 and solving with zero initial conditions we get,

$$\frac{\partial^2 U(s, z)}{\partial z^2} = \frac{s^2}{v^2} U(s, z) \quad (4.5)$$

$$U(s, z) = Ae^{-\frac{s}{v}z} + Be^{\frac{s}{v}z} \quad (4.6)$$

As evident from Equation 4.6, triggering each stack of the PA generates stress waves in both  $+z$  and  $-z$  directions. Optimizing the triggering delay between the stacks can enable the  $-z$  stress wave of the upper stack can be utilized to dampen out the  $+z$  stress wave waves of the lower stacks as shown in [3]. The minimum triggering delay between two adjacent stacks is defined by the propagation delay of the stress wave through one stack. For the PPA40L actuator, each stack is  $20 \text{ mm}$  in length. Hence the minimum delay is  $\frac{0.02 \text{ m}}{2355 \text{ m/s}} = 8.5 \mu\text{s}$ . This method can be experimentally implemented by generating two time-delayed actuation pulses from the function generator as shown in Figure 4-2. Experimental results for this method of individual control of stacks implemented for the PPA40L actuator are presented in Section 3, Chapter 5. For PAs with a greater number of stacks such as the Cedrat<sup>®</sup> PPA120XL actuator used for the EDISON FMS which has 6

such stacks, a time-sequence driving circuit would be required to coordinate the time delay between each stack [20].

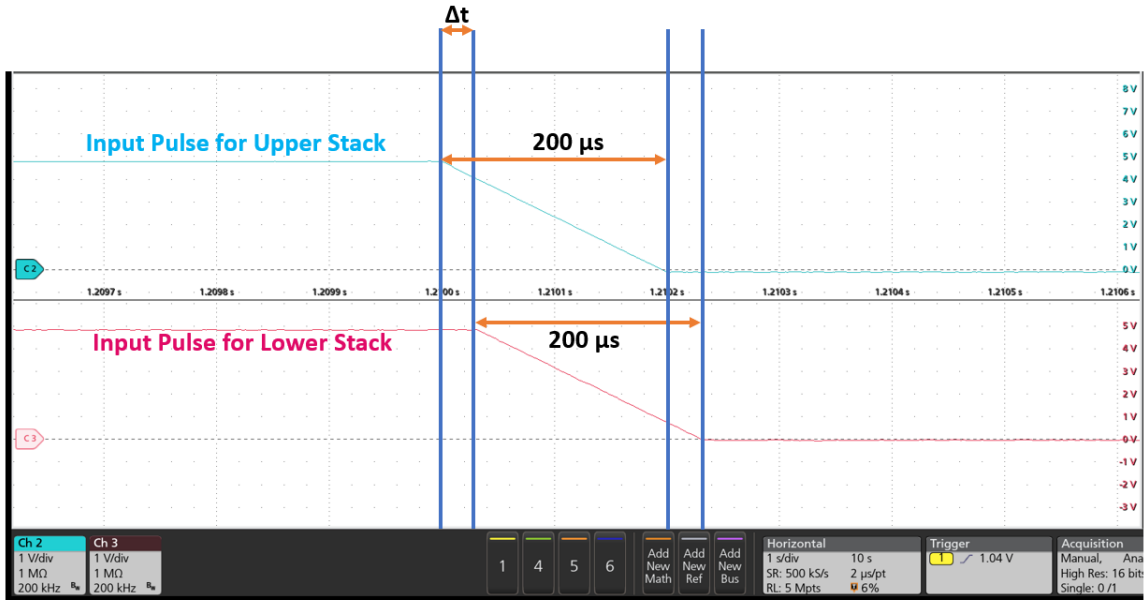


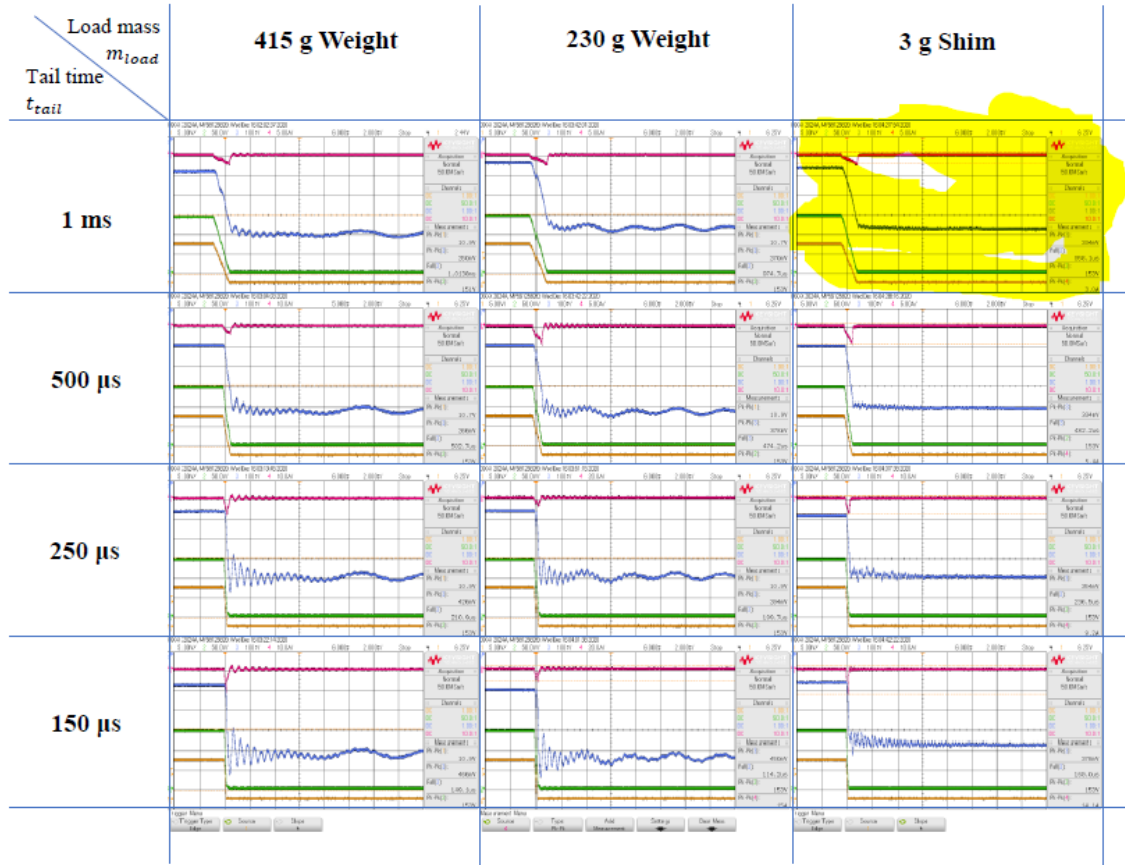
Figure 4-2: Time-shifted pulse for Sequential Triggering Method from the Tektronix AFG31022 Arbitrary Function Generator.

## 4.2 Input Shaping Method

The input shaping method is a vibration damping method where the knowledge of the natural or resonance frequency of the system enables us to modify the input signal such as to reduce the overshoot/undershoot in the system [25]. The rationale to apply this method for this study stems from the primary hypothesis, which states each stack of a PA is exposed to different mechanical conditions during the actuation process and hence applying an input signal customized to each stack would enable us to optimize the net displacement curve. Equation 2.5 describes how the resonance frequency of an oscillating body is correlated to the total mass oscillating with it. As explained in Section 2.4.2, the lower stack pushes a greater mass during the actuation process than the upper stack and hence has a lower

resonance frequency. Therefore, if we actuate both the stacks with a signal with the same rate of change of voltage  $dv/dt$ , the lower stack will be operating closer to its resonance frequency causing it to be the source of greater oscillations. This is evident from the experimental curves in Section 5.2 where we observe almost double the undershoot for the lower stack as compared to the upper stack when each of them is actuated individually while shorting the other through a resistor.

Figure 4-3 of experiments conducted for the PPA40L actuator in [3] shows us how the oscillations in the PA displacement curve increase with mass and  $dv/dt$ . Note that during these experiments each PA stack received the same input signal. These responses give us an understanding of how the oscillations in an individual stack as well could be reduced by driving it with a reduced  $dv/dt$  as we are operating it further away from its resonance frequency. The simplest form of input shaping for our application would be to actuate the two stacks with input signals with different  $dv/dt$ . Since the lower stack is the source of greater vibrations, a more damped response can be obtained by compensating the higher mass by actuating it with an input signal with lower  $dv/dt$ . This is implemented by increasing the fall time of its actuating signal. Again, reducing the  $dv/dt$  of the actuating signal might compromise the overall switching time and hence we need to strike a balance between the two parameters. Section 5.3 shows and discusses the experimental responses when both the stacks are actuated with input signals of varying fall times.



Curve Legend:

- Pink -  $I_{piezo}$ , actuator driving current, 5/10/20 A/div
- Blue -  $V_{disp.sensor.out}$ , displacement sensor output/actuator displacement, 100 mV/div is equivalent to 12.5  $\mu$ m/div for travel curve  $d_{piezo}$
- Green -  $V_{piezo}$ , actuator driving voltage, 50 V/div
- Yellow -  $V_{signal}$ , driver input signal, 5 V/div

Figure 4-3: Experimental curves for the PPA40L actuator provided in [3] showing how oscillations increase with an increase in both mass and  $dv/dt$  of the input signal.

### 4.3 Chapter Summary

This chapter describes the theory for the two individual piezoelectric stack control methods explored in this work. The sequential triggering method introduces a delay in the order of  $\mu$ s between consecutive stack actuation. It uses the negative  $z$ -direction stress wave of one stack to dampen out the oscillations due to the other stack. The input shaping method

aims to reduce the oscillations in the response by triggering the lower stack with a higher fall time to operate it further away from its resonance frequency.

## CHAPTER 5      EXPERIMENTAL IMPLEMENTATION OF CONTROL METHODS

This chapter describes the experimental test setup, results, and conclusions after implementing the two individual stack control methods.

### 5.1 Experimental Setup

#### 5.1.1 Setup for driving piezo actuator

Figure 5-1 shows the hardware setup used to implement the experimental circuit to test the control methods described in the previous chapter. It includes a two-channel function generator, two power amplifiers, two damping resistors, the PPA40L actuator, a displacement sensor, voltage and current sensors, and an oscilloscope. A detailed description of each piece of equipment is given in the following sections of this chapter.

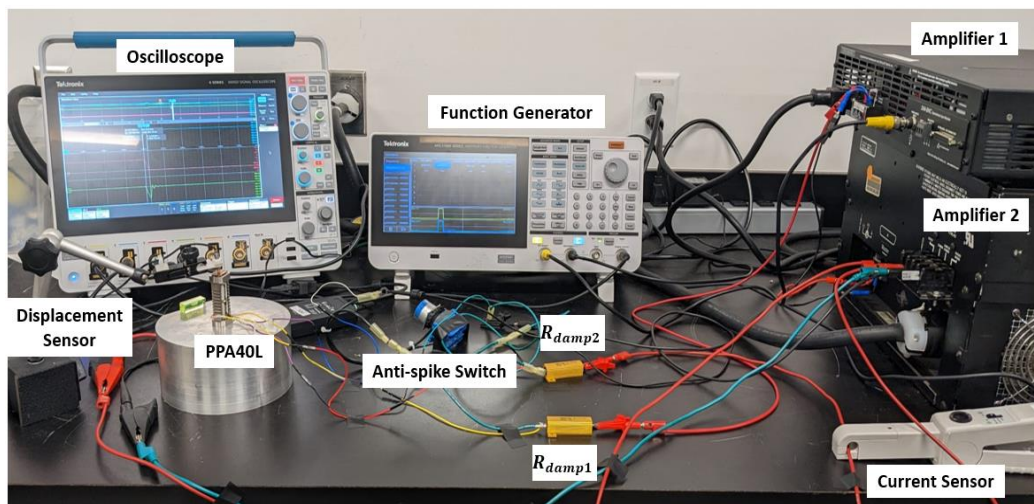


Figure 5-1: Experimental test setup.

#### 5.1.1.1 Separate leads for each stack

Most commercially available multi-stack piezoelectric actuators are designed for all the stacks to be driven by the same actuating signal. Hence, all the positive leads and negative leads are soldered to form two composite leads as shown for the PPA40L actuator in Figure 5-2(right). The first step to individually control each stack of the actuator was to desolder these leads and connect four leads for the positive and negative connections of the two stacks. This is depicted in Figure 5-2(left).

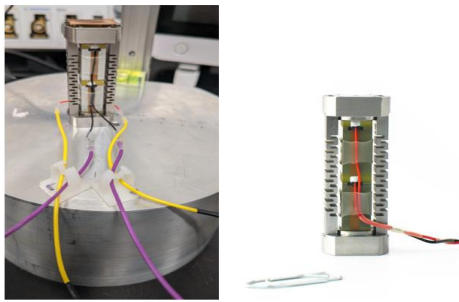


Figure 5-2: PPA40L actuator with individual leads for each stack (left), PPA40L actuator [17] with positive leads connected and negative leads connected as received from the manufacturer (right).

#### 5.1.1.2 Function Generator

The individual control of stacks of the PPA40L actuator requires two controllable pulsed actuation signals and the option to manually trigger them simultaneously. The Tektronix® AFG31022 Arbitrary Function Generator [26] is suitable for this purpose. The Tektronix® AFG31022 is an arbitrary function generator that features a bandwidth of up to 25 MHz, a maximum sampling rate of 250 MS/s, and two independent channels that can generate synchronized or independent signals. It can generate pulsed waveforms of 0-5 V amplitude of adjustable pulse width, rise time, and fall time. Figure 5-3 shows two

amplified pulse signals from the two channels of this function generator measured across two capacitor loads of  $4.7 \mu\text{F}$ , which is very close to the  $4.4 \mu\text{F}$  capacitance of each individual stack of the PPA40L actuator. Both channel outputs are manually triggered through the single trigger button on the front panel of the function generator. Variations of these pulsed waveforms are used as actuating signals for each stack of the actuator during the experiments.

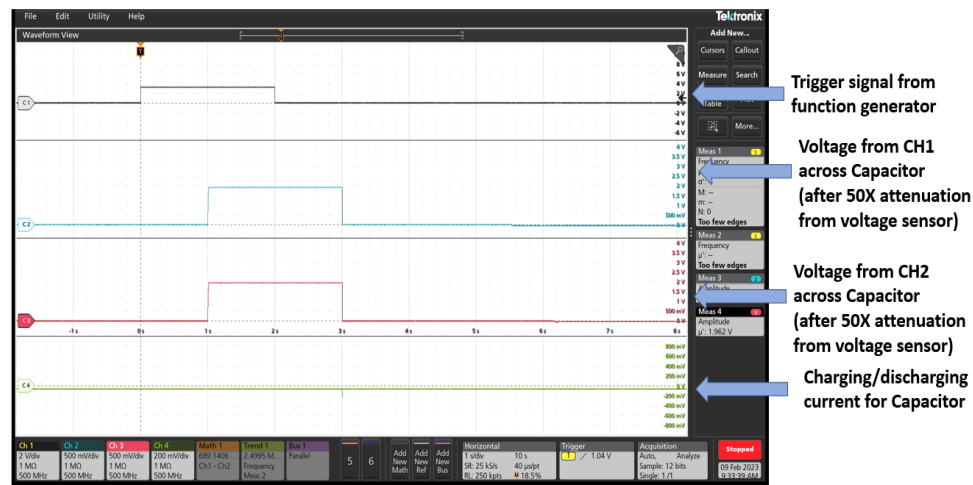


Figure 5-3: Amplified waveforms from 2 channels of the function generator measured across capacitor loads.

### 5.1.1.3 Amplifiers

Two power amplifiers are required to drive the two stacks of the PPA40L actuator independently. The AE Techron<sup>®</sup> 7224 (Figure 5-4 a) and the AE Techron<sup>®</sup> 8524 (Figure 5-4 b) models of power amplifiers are used in the experiments. The AE Techron<sup>®</sup> 7224 is a linear, four-quadrant amplifier with 0-300 kHz bandwidth and can output a peak power of 6 kW. In the voltage mode, it has a variable gain of up to 20 V/V. The AE Techron<sup>®</sup> 8524 is a 3-phase power amplifier rated for 208 V AC, 16 A with a fixed gain of 20 V/V.

Neither of these amplifiers are optimized for the purpose of driving a PA but are suitable for this task as demonstrated here, albeit with continuous power ratings well excess of what is required. The more efficient method to drive the PA stacks would be through a multi-channel power amplifier circuit built on a compact PCB board and fed through a capacitor bank since continuous current is not required for charging or discharging the PA. To prevent voltage spikes across the PA terminals during the power-up transients of the amplifiers [3], an anti-spike switch is connected in parallel to each stack. This switch shorts out the PA stacks during the switching-on of the amplifiers and brings them back into the circuit once the transients have settled.

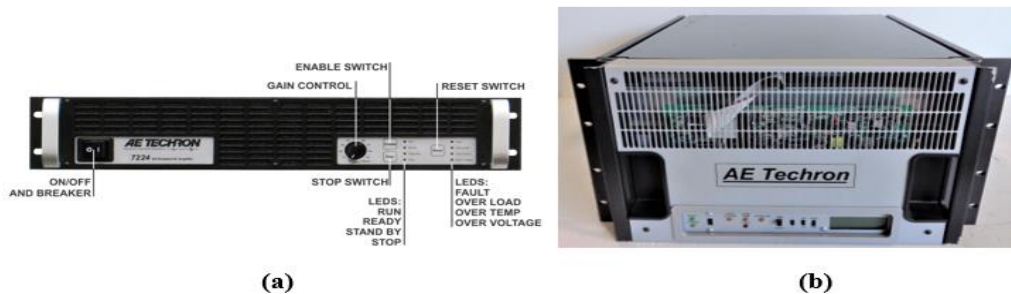


Figure 5-4: (a) AE Techron<sup>®</sup> 7224 Power Amplifier (b) AE Techron 8524<sup>®</sup> Power Amplifier.

#### 5.1.1.4 Displacement Sensor

The experimental displacement travel curves in Figure 5-6 are obtained with an eddy current displacement sensor system (ECL101-U5-SAM-3.0) manufactured by Lion Precision<sup>®</sup>. It consists of the ECL101 sensor driver (Figure 5-5a) powered by a 20 V battery pack along with the U5 sensing probe (Figure 5-5b). A battery pack was chosen over a power supply to minimize noise being coupled into the measurement. An eddy current

displacement sensor works by passing an alternating current through its probe, which generates an alternating magnetic field near the target. This induces eddy currents in the target, which changes the mutual impedance sensed by the probe. The amount of change in impedance would depend on the distance between the target and the probe [3]. For correct sensing, a minimum target thickness is required to allow sufficient penetration of the inductive probe's electromagnetic field. For copper, this value is 0.2 mm [27]. The sensing system has a near gap of 250  $\mu\text{m}$ , a range of 1250  $\mu\text{m}$ , and a sensitivity of 8.0 mV/ $\mu\text{m}$ .

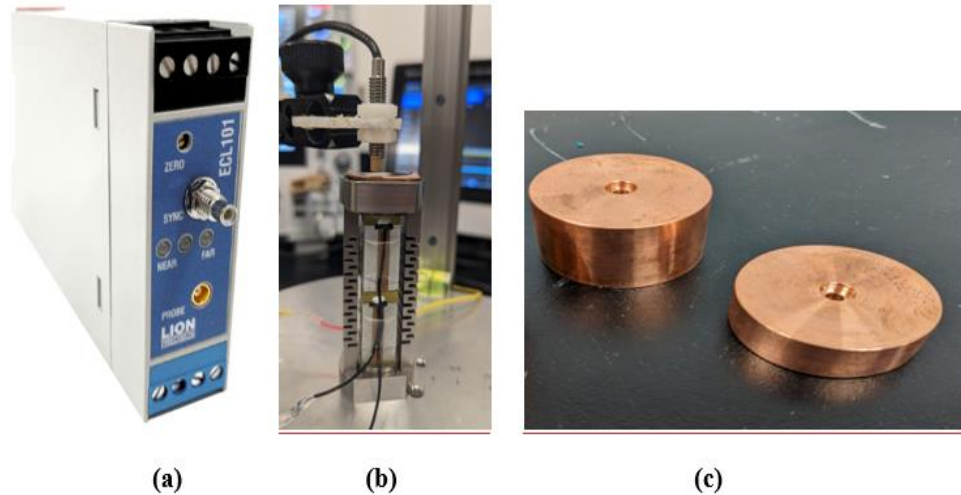


Figure 5-5: (a) Displacement sensor driver Lion Precision® ECL101 (b) Displacement sensor U5 probe positioned over a 1 g copper shim target on top of the PPA40L actuator (c) Payload masses designed to emulate contact weights of a circuit breaker.

#### 5.1.1.5 Current Sensor

To sense the charging/discharging current of the actuator during the tests, a Keysight® 1146B AC/DC current probe with a bandwidth of 100 kHz is hooked around the

wire connected to the positive terminal of either stack. The sensitivity of this current probe is kept at 100 mV/A.

### 5.1.1.6 Contact Masses

Figure 5-5c shows the 115 g and 220 g copper contact masses designed to emulate the contact weights of the circuit breaker. These masses are bolted on top of the PPA40L during experiments to study the variation of response with payload. Lock washers are used to prevent vibrations due to the connection between the PA and the masses. These masses along with a 1 g copper shim also serve as the target for the displacement sensor probe.

## 5.2 Experimental Displacement Curve when each Stack is Individually Triggered

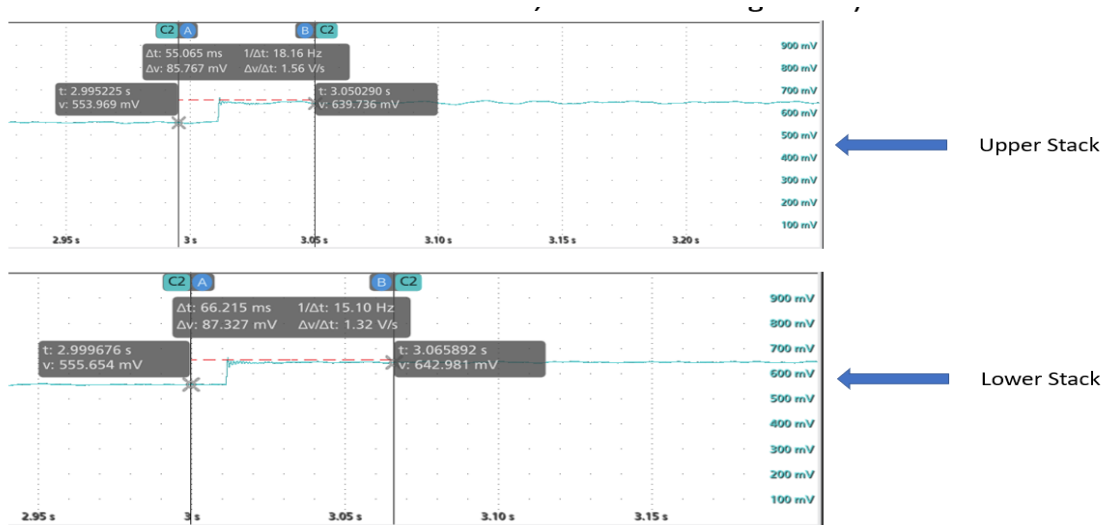


Figure 5-6: Displacement Sensor output in the compression region when each stack is individually triggered.

Figure 5-6 illustrates the experimental output of the displacement sensor in the compression region when each stack is individually triggered with an actuation voltage of 81 V. We assume the displacement response to be linear and hence superposition principle

is valid. The fall time or tail time of the actuation voltage is defined as the time the actuation voltage takes to drop from 100% to 0% of its value. It is illustrated in Figure 5-7. The distance of the copper shim target from the displacement sensor decreases during the elongation process and increases during the compression process. As mentioned in Section 5.1.1.4, the sensitivity of the displacement sensor is 8 mV/ $\mu\text{m}$ . The initial distance between the target and the displacement sensor is 331  $\mu\text{m}$  which is 81  $\mu\text{m}$  from the near gap of the sensor. For better visibility, the experimental data is plotted in MATLAB. Figure 5-8 illustrates this MATLAB plot where the blue response curve is the displacement curve when the upper stack is actuated by a voltage of 81 V and fall time of 200  $\mu\text{s}$  while the lower stack is shorted through a resistor. The red response curve is the displacement curve when the lower stack is actuated by a voltage of 81 V and fall time of 200  $\mu\text{s}$  while the upper stack is shorted through a resistor. A difference in responses is observed especially in the undershoot region. The upper stack has a percentage undershoot of 12.5% while the lower stack has a percentage undershoot of 21.2%. Hence, close to double the undershoot is observed for the lower stack as compared to the upper stack. This strengthens the hypothesis that each stack in a multi-stack PA should be controlled individually as they have different responses owing to their different positions in the stack. We also noticed a negligible difference between the two stacks in the overshoot region. This may be due to the compression constraints in the prestressed PA as observed in [3]. The undershoot region is more significant for us as this is when the contacts of the HCB come closer to each other during the actuation oscillations. Hence, a high undershoot will increase the risk of restriking in the HCB. It should also be noted over here, that for a PA with greater number of stacks - such as the PPA120XL used for the EDISON fast mechanical switch which has

six piezoelectric stacks - the difference in undershoot between the higher and lower stacks is expected to further increase.

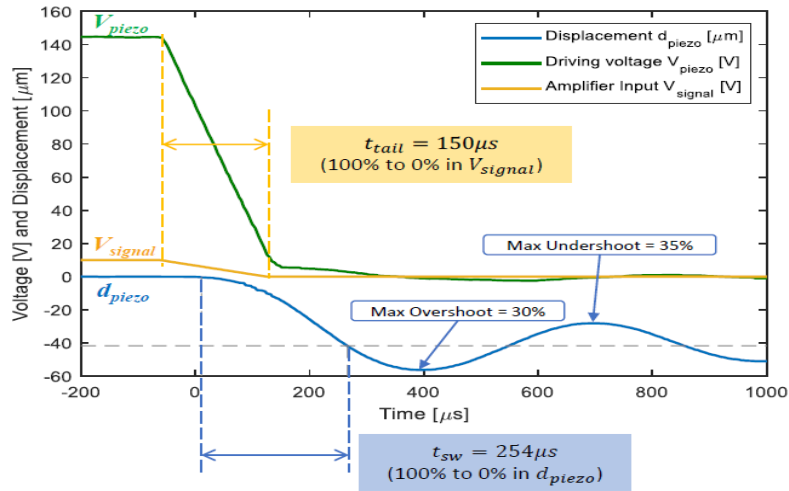


Figure 5-7: Illustrations of fall time (or tail time  $t_{tail}$ ) and switching time  $t_{sw}$  as defined in [3]

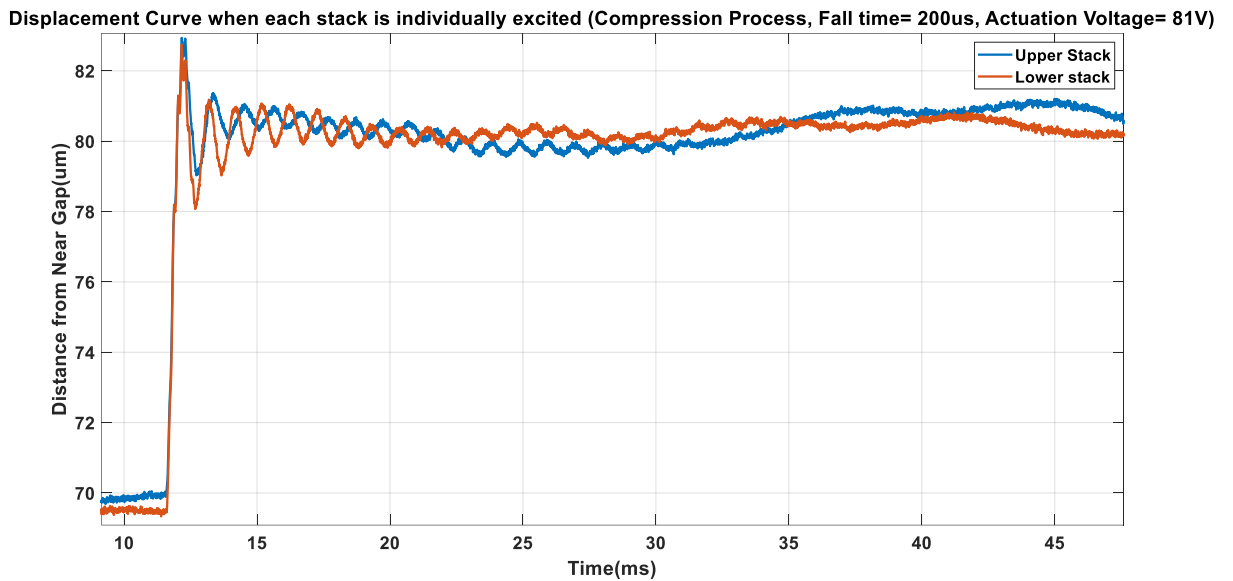


Figure 5-8: Experimental displacement curves plotted on MATLAB for better clarity of overshoot/undershoot region.

### 5.3 Experimental Results and Discussion

#### 5.3.1 Effect of varying $dv/dt$ of lower stack (Method 1)

To test control method 1, the two stacks of the PPA40L actuator are triggered by a voltage of 95 V and the fall time of the lower stack is varied. The fall time of the upper stack is kept constant at 200  $\mu$ s. Figure 5-9 shows the experimental displacement travel curve of the contact mass on top of the actuator. The fall time of the lower stack is increased from 200  $\mu$ s to 240  $\mu$ s and 520  $\mu$ s. As evident from the figure, the increase in the fall time or decrease in  $dv/dt$  of the lower stack reduces the percentage undershoot of the net response. This reduces the risk of re-striking of the arc when the circuit breaker contacts are separating during a fault. Table 5-1 and Table 5-2 gives a quantitative description of the decrease in percentage undershoot and increase in switching time on implementing control method 1.

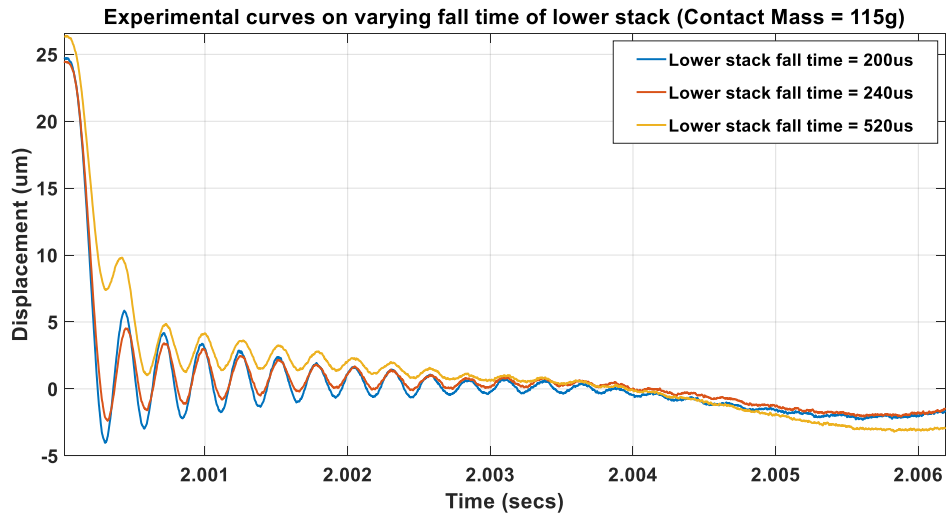


Figure 5-9: Experimental displacement travel curves to illustrate the impact of varying  $dv/dt$  of the lower stack.

Table 5-1: Experimental Data Table for Undershoot (%) for Method 1.

<b>Payload Mass (g)</b>	<b>Fall time of Lower Stack (<math>\mu\text{s}</math>)</b>		
	<b>200</b>	<b>240</b>	<b>520</b>
<b>1</b>	4.28	3.93	1.93
<b>115</b>	5.85	4.50	Overdamped
<b>220</b>	9.59	8.65	6.20

Table 5-2: Experimental Data Table for Switching Time (10-90% of steady-state) ( $\mu\text{s}$ ) for Method 1.

<b>Payload Mass (g)</b>	<b>Fall time of Lower Stack (<math>\mu\text{s}</math>)</b>		
	<b>200</b>	<b>240</b>	<b>520</b>
<b>1</b>	198	210	328
<b>115</b>	130	142	426
<b>220</b>	138	156	472

### 5.3.2 *Effect of sequential triggering (Method 2)*

To test control method 2, the two stacks of the PPA40L actuator are triggered by a voltage of 95 V and the delay between the actuation of the individual stacks is varied. The fall time of the upper stack and the lower stack is kept constant at 200  $\mu\text{s}$  but the lower stack is triggered after a variable delay. Figure 5-10 shows the experimental displacement travel curve of the contact mass on top of the actuator. The delay is increased from simultaneous triggering (no delay) to 16  $\mu\text{s}$  and 48  $\mu\text{s}$ . An increase in the delay is accompanied by a slight reduction in the percentage overshoot of the response. However, the percentage undershoot remains nearly constant. Relative to method 1, the benefits of method 2 alone are hence limited. The next section analyses the benefits of combining the

two methods to get an improved response. Table 5-3 and Table 5-4 gives a quantitative description of the decrease in percentage overshoot and increase in switching time on implementing control method 1.

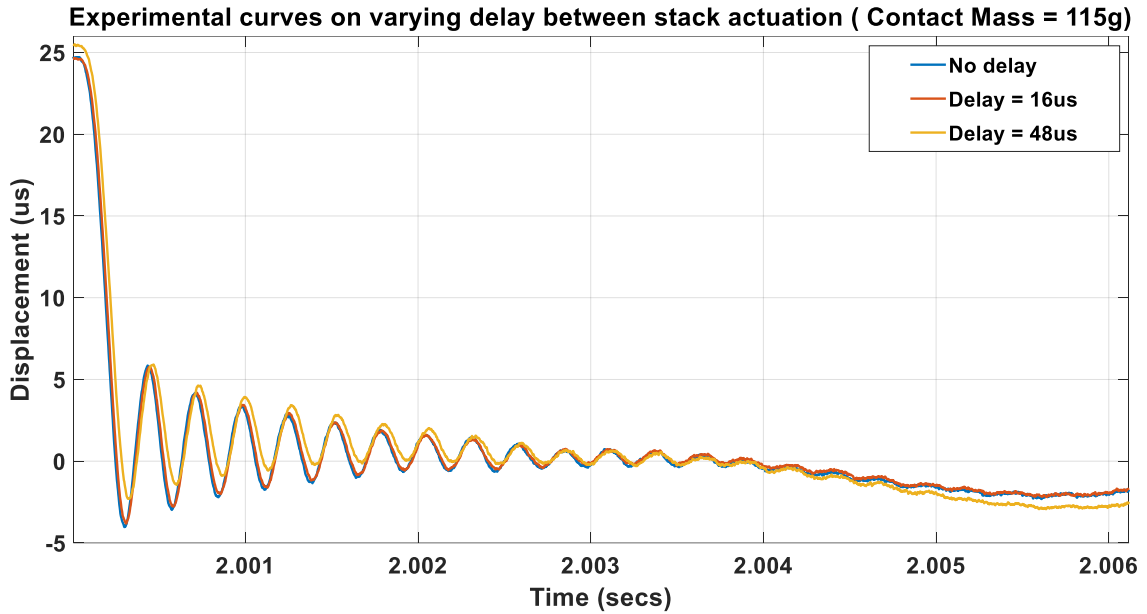


Figure 5-10: Experimental displacement travel curves to illustrate the impact of varying delay between stack actuation.

Table 5-3: Experimental Data Table for Overshoot (%) for Method 2.

Payload Mass (g)	Delay between stack actuation ( $\mu\text{s}$ )		
	No delay	16	48
1	4.71	3.20	2.79
115	4.03	3.82	2.30
220	5.79	4.65	1.22

Table 5-4: Experimental Data Table for Switching Time (10-90% of steady-state) ( $\mu\text{s}$ ) for Method 2.

<b>Payload Mass (g)</b>	<b>Delay between stack actuation (<math>\mu\text{s}</math>)</b>		
	<b>No delay</b>	<b>16</b>	<b>48</b>
<b>1</b>	198	310	308
<b>115</b>	130	130	142
<b>220</b>	138	142	150

### 5.3.3 *Effect of combining method 1 and method 2*

The final experiment was to analyze the displacement response of the actuator on combining control methods 1 and 2. Figure 5-11 compares the experiment results of no control, control method 1, control method 2, and a combination of 1 and 2. It can be observed from the figure that methods 1 and 2, when individually applied, help to reduce the oscillations by approximately 50% which may not be an adequate reduction for a circuit breaker application. To combine the two methods, the fall time of the lower stack is increased to 520  $\mu\text{s}$  and a delay of 48  $\mu\text{s}$  is also introduced before actuating the lower stack. The response represented by the violet curve in Figure 5-11 shows a critically damped response curve with no undershoot or overshoot and with a switching time of just 462  $\mu\text{s}$ . Thus, combining the two control methods described in this work shows the most promising results.

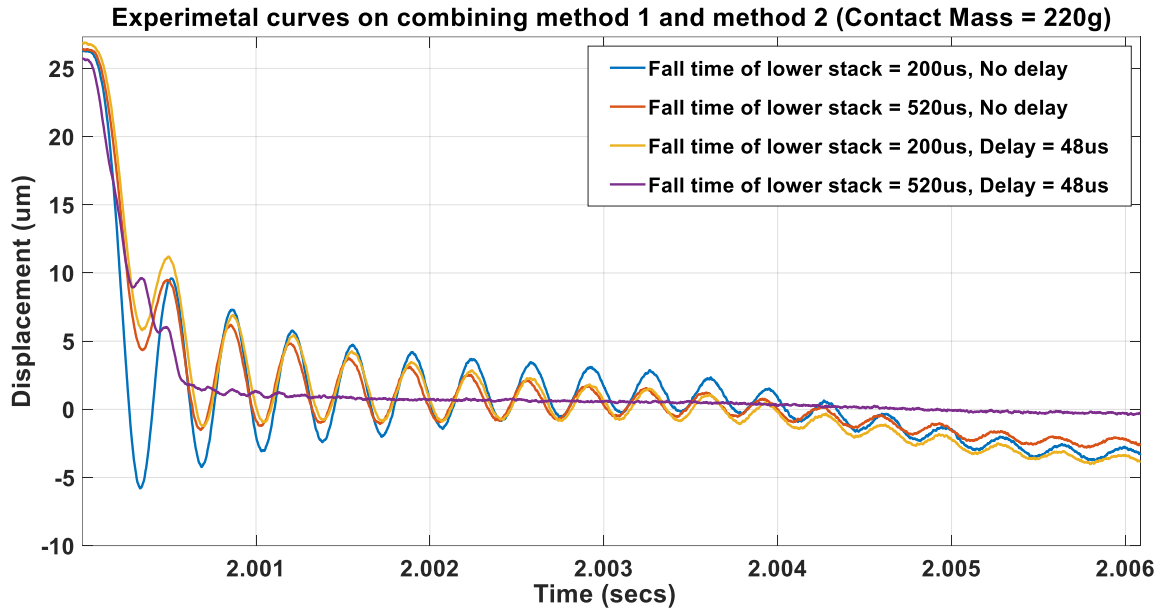


Figure 5-11: Experimental displacement travel curves to compare the impact of method 1 (red), method 2 (yellow) and combination of methods 1 and 2 (violet).

## 5.4 Chapter Summary

This chapter describes the experimental setup, results and conclusions when the two individual stack control methods are applied. Increasing the fall time of the actuating voltage of the lower stack reduces the percentage undershoot significantly. The sequential triggering method reduces the percentage overshoot of the response while little change is observed in the undershoot. A combination of both these methods shows great potential by leading to a critically damped response with a switching time of just 426  $\mu$ s.

## CHAPTER 6 CONCLUSION AND FUTURE WORK

### 6.1 Conclusion

This research focuses on understanding and analyzing two open-loop methods for the control of individual stacks of a piezoelectric actuator in order to improve its displacement travel curve during actuation for the application of fast mechanical switches for hybrid circuit breakers. The main contributions of this research are: (1) the proposed hypothesis of individual stack control has been validated through experimental tests; (2) building a digital model to better understand the dynamics and control of the system (3) the proposed digital simulation model of the system captures the falling edge and the frequency of oscillations in the displacement curve well. The mismatch in the amplitude of oscillations can be explained by the compressive constraints due to the pre-stressing frame in the experimental setup which cannot be replicated in the simulation model; (4) the two control strategies namely- varying the rate of change of voltage  $dv/dt$  of the actuation voltage for the lower stack and sequential triggering method have been experimentally tested. The first method reduced the percentage undershoot of the response significantly and hence will help to reduce the risk of restriking of the arc during opening of the circuit breaker. Combining both the methods for the PPA40L actuator had extremely promising results as the displacement curve was critically damped with a switching time of just 462  $\mu\text{s}$ .

Applying these control methods to larger piezoelectric actuators such as the PPA120XL used in the EDISON project would require a further study of the digital model

and designing a hardware implementation circuit. These aspects will be discussed in the following section.

## **6.2 Future Work**

Future work concerning the research presented in this thesis could be in the following areas:

1. The digital simulation model can be further studied to analyze if the pre-stressing force on the piezoelectric stacks can be represented. This would reduce the error in capturing the amplitude of oscillation during the actuation process. The model can also be extended to the PPA120XL driving circuit used in the EDISON circuit breaker which has six piezoelectric stacks.
2. To drive the six-stack actuator using these control methods, a driving circuit will have to be designed. This could be a DSP and FPGA-based circuit, which stores and outputs the ideal control waveforms to each stack through six output channels. Power amplifiers, driving the piezoelectric actuators and fed from a capacitor bank, could be integrated into the same circuit.
3. The benefits or feasibility of applying the actuating voltage in steps can be explored. This could potentially further reduce the oscillations in the displacement travel curve of the actuator.
4. The significant reduction in oscillations when a combination of both the control methods proposed in this work are applied is an empirical result. Studying and developing an analytical relationship between this method and the response would

make it easier to extend it to piezoelectric actuators other than the one used in this study.

5. To be able to model the piezoelectric stacks of the actuator correctly it is essential to know the material properties better. A potential area to work on would be to explore new types of piezoelectric actuators based on new materials or geometries.

## APPENDIX A. TERMS USED TO DESCRIBE PIEZOELECTRIC ACTUATOR

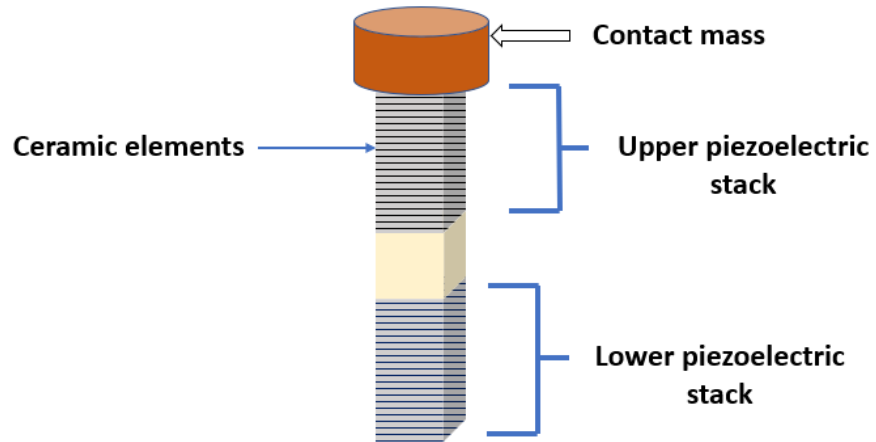


Figure A-1: Diagram showing components of the piezoelectric actuator and the terminology used to refer to them in this thesis.

## REFERENCES

- [1] M. Tousi *et al.*, “A Piezoelectric Actuator Optimized for Fast Mechanical Switch Applications,” in *2022 IEEE 67th Holm Conference on Electrical Contacts (HLM)*, IEEE, Oct. 2022, pp. 1–6. doi: 10.1109/HLM54538.2022.9969833.
- [2] M. Goldfarb and N. Celanovic, “Modeling piezoelectric stack actuators for control of micromanipulation,” *IEEE Control Syst*, vol. 17, no. 3, pp. 69–79, Jun. 1997, doi: 10.1109/37.588158.
- [3] C. Xu, “CONTROL STRATEGIES FOR PIEZOELECTRICALLY ACTUATED FAST MECHANICAL DISCONNECT SWITCHES FOR HYBRID CIRCUIT BREAKERS,” Georgia Institute of Technology, Atlanta, 2021.
- [4] P. Ronkanen, P. Kallio, and H. N. Koivo, “Current control of piezoelectric actuators with power loss compensation,” in *IEEE/RSJ International Conference on Intelligent Robots and System*, IEEE, pp. 1948–1953. doi: 10.1109/IRDS.2002.1044041.
- [5] L. Graber *et al.*, “EDISON: A New Generation DC Circuit Breaker.”
- [6] L. Qi *et al.*, “Solid-State Circuit Breaker Protection for DC Shipboard Power Systems: Breaker Design, Protection Scheme, Validation Testing,” *IEEE Trans Ind Appl*, vol. 56, no. 2, pp. 952–960, Mar. 2020, doi: 10.1109/TIA.2019.2962762.
- [7] R. Rodrigues, Y. Du, A. Antoniazzi, and P. Cairoli, “A Review of Solid-State Circuit Breakers,” *IEEE Trans Power Electron*, vol. 36, no. 1, pp. 364–377, Jan. 2021, doi: 10.1109/TPEL.2020.3003358.
- [8] *Piezoelectric Ceramics: Principles and Applications*, Second Edition. APC International, Ltd.
- [9] J. Minase, T.-F. Lu, B. Cazzolato, and S. Grainger, “A review, supported by experimental results, of voltage, charge and capacitor insertion method for driving piezoelectric actuators,” *Precis Eng*, vol. 34, no. 4, pp. 692–700, Oct. 2010, doi: 10.1016/j.precisioneng.2010.03.006.
- [10] “176-1987 - IEEE Standard on Piezoelectricity,” 1988.
- [11] Frank Claeysen, Christian Belly, Ronan Le Letty, and Mathieu Bagot, “Dynamic strain limits of Amplified Piezo Actuators,” Jun. 2010. [http://metrology-spb.ru/upload-files/CEDRAT\\_TECHNOLOGIES/English\\_articles\\_PDF/Dynamic\\_strain\\_limits\\_of\\_APA.pdf](http://metrology-spb.ru/upload-files/CEDRAT_TECHNOLOGIES/English_articles_PDF/Dynamic_strain_limits_of_APA.pdf)
- [12] “Amplified piezo actuator - APA30uXS,” Jun. 2022. <https://www.cedrat-technologies.com/fileadmin/datasheets/APA30uXS.pdf>

- [13] C. Xu, T. Damle, and L. Graber, "A Survey on Mechanical Switches for Hybrid Circuit Breakers," in *2019 IEEE Power & Energy Society General Meeting (PESGM)*, IEEE, Aug. 2019, pp. 1–5. doi: 10.1109/PESGM40551.2019.8973674.
- [14] C. Xu *et al.*, "Piezoelectrically Actuated Fast Mechanical Switch for MVDC Protection," *IEEE Transactions on Power Delivery*, vol. 36, no. 5, pp. 2955–2964, Oct. 2021, doi: 10.1109/TPWRD.2020.3030869.
- [15] "Amplified Piezo Actuator APA1000XL," *Cedrat Technologies*, Jun. 2022. <https://www.cedrat-technologies.com/fileadmin/datasheets/APA1000XL.pdf> (accessed Mar. 03, 2023).
- [16] "Parallel Pre-stressed Actuator PPA120XL," *Cedrat Technologies*, Feb. 2022. <https://www.cedrat-technologies.com/fileadmin/datasheets/PPA120XL.pdf> (accessed Mar. 03, 2023).
- [17] "Parallel Pre-stressed Actuator - PPA40L," *Cedrat*. <https://www.cedrat-technologies.com/en/products/product/PPA40L.html> (accessed Mar. 01, 2023).
- [18] "TOKIN - Resin Coated Multilayer Piezoelectric Actuators," *Micromechatronics, Inc.* <https://www.mmech.com/tokin-actuators/nec-tokin-resin-coated/nec-ae1010d16f> (accessed Mar. 04, 2023).
- [19] "Piezoelectric Actuators Factory Verification for PPA40L," Jan. 2020.
- [20] X. Ba, Q. Pan, B. Ju, and Z. Feng, "Ultrafast Displacement Actuation of Piezoelectric Stacks With Time-Sequence," *IEEE Transactions on Industrial Electronics*, vol. 64, no. 4, pp. 2955–2961, Apr. 2017, doi: 10.1109/TIE.2016.2631119.
- [21] D. Kohl, C. Kerschner, and G. Schitter, "Automatic fourier synthesis based input-shaping for scanning piezo-electric actuators," in *2017 IEEE International Conference on Advanced Intelligent Mechatronics (AIM)*, IEEE, Jul. 2017, pp. 1083–1088. doi: 10.1109/AIM.2017.8014163.
- [22] M. Bazghaleh, S. Grainger, and M. Mohammadzaheri, "A review of charge methods for driving piezoelectric actuators," *J Intell Mater Syst Struct*, vol. 29, no. 10, pp. 2096–2104, Jun. 2018, doi: 10.1177/1045389X17733330.
- [23] C. Xu, Z. Jin, M. Tousi, and L. Graber, "Critical Damping in Travel Curves of Piezoelectrically Actuated Fast Mechanical Switches for Hybrid Circuit Breakers," *IEEE Transactions on Power Delivery*, vol. 37, no. 5, pp. 3873–3884, Oct. 2022, doi: 10.1109/TPWRD.2021.3140159.
- [24] "Multilayer Piezoelectric Actuators User Manual," Jan. 2021. [https://www.mmech.com/images/stories/Standard\\_Products/Tokin/Multilayer-Piezoelectric-Actuator-User-Manual-Rev-1\\_1.pdf](https://www.mmech.com/images/stories/Standard_Products/Tokin/Multilayer-Piezoelectric-Actuator-User-Manual-Rev-1_1.pdf)

- [25] S. Kapucu, G. Alici, and S. Bayseç, “Residual swing/vibration reduction using a hybrid input shaping method,” *Mech Mach Theory*, vol. 36, no. 3, pp. 311–326, Mar. 2001, doi: 10.1016/S0094-114X(00)00048-3.
- [26] “x AFG31000 Series Arbitrary Function Generator User’s Manual.”
- [27] “What is the Minimum Recommended Target Thickness for Eddy-Currents?,” *Lion Precision*, 2008. <https://www.lionprecision.com/minimum-recommended-eddy-current-target-thickness/> (accessed Mar. 01, 2023).
- [28] “How does stiffness affect piezo output force and displacement?,” <https://www.motioncontroltips.com/how-does-stiffness-affect-piezo-output-force-and-displacement/>.